Convergence of Fourier-based time methods for turbomachinery wake passing problems

Adrien Gomar[a,1,*], Quentin Bouvy[a,2], Frédéric Sicot[a,3], Guillaume Dufour[b,4], Paola Cinnella[c,5], Benjamin François[a,d,1]

[a]*CERFACS, CFD Team, 42 avenue Gaspard Coriolis, 31057 Toulouse cedex 1, France*
[b]*Université de Toulouse, Institut Supérieur de l'Aéronautique et de l'Espace (ISAE), 10 avenue Edouard Belin, 31400 Toulouse, France*
[c]*DynFluid Lab., Arts et Métiers ParisTech, 151 Boulevard de l'Hopital, 75013 Paris, France*
[d]*Airbus Operations S.A.S., 316 route de Bayonne, 31060 Toulouse Cedex 9, France*

Abstract

The convergence of Fourier-based time methods applied to turbomachinery flows is assessed. The focus is on the harmonic balance method, which is a time-domain Fourier-based approach standing as an efficient alternative to classical time marching schemes for periodic flows. In the literature, no consensus exists concerning the number of harmonics needed to achieve convergence for turbomachinery stage configurations. In this paper it is shown that the convergence of Fourier-based methods is closely related to the impulsive nature of the flow solution, which in turbomachines is essentially governed by the characteristics of the passing wakes between adjacent rows. As a result of the proposed analysis, *a priori* estimates are provided for the minimum number of harmonics required to accurately compute a given turbomachinery configuration. Their application to several contra-rotating open-rotor configurations is assessed, demonstrating the practical interest of the proposed methodology.

[*]Corresponding author

Email addresses: `adrien.gomar@gmail.com` (Adrien Gomar), `quentin.bouvy@cerfacs.fr` (Quentin Bouvy), `frederic.sicot@cerfacs.fr` (Frédéric Sicot), `guillaume.dufour@isae.fr` (Guillaume Dufour), `paola.cinnella@ensam.eu` (Paola Cinnella), `benjamin.francois@cerfacs.fr` (Benjamin François)

[1]Ph.D. Student
[2]Study Engineer
[3]Senior Researcher
[4]Associate Professor
[5]Professor

1. Introduction

The industrial design of turbomachinery is usually based on steady flow analysis, for which the reference simulation tool are the three-dimensional Reynolds-Averaged Navier–Stokes (RANS) steady computations. However, this approach finds its limits when unsteady phenomena become dominant. In such a context, engineers now need to account for unsteady-flow effects as early as possible in the design cycle, which makes efficiency of unsteady computations a key issue. A specificity of turbomachinery flows is their periodicity, at least as far as the mean field properties are considered.

Fourier-based time methods for periodic flows have undergone major developments in the last decade (see He [1] for instance) as they allow to reduce the computational cost of unsteady simulations as compared to standard time-marching techniques. The basic idea is to decompose the time-dependent flow variables into Fourier series, which are then injected into the equations of the problem. The time-domain problem is thus made equivalent to a frequency-domain problem, where the complex Fourier coefficients are the new unknowns. At this point, two strategies coexist to obtain the solution. The first one is to directly solve the Fourier coefficients equations, using a dedicated frequency-domain solver, as proposed by He and Ning [2, 3]. The second strategy is to cast the problem back to the time domain using the inverse Fourier transform, as proposed by Hall [4, 5] with the Harmonic Balance (HB) method. The unsteady time-marching problem is thus transformed into a set of steady equations coupled by a source term that represents a spectral approximation of the time-derivative of the initial equations. The main benefit of solving in the time domain is that such a methodology can be easily implemented in an existing RANS solver, taking advantage of all classical convergence-accelerating techniques for steady state problems. The HB approach has demonstrated a

significant reduction of the CPU time, typically one to two orders of magnitude [6, 7, 8].

Efficiency of the HB method results from a trade-off between accuracy and costs requirements. On one hand, the accuracy of Fourier-based time methods depends on the number of harmonics used to represent the frequency content of the time signal; on the other hand, computational costs and memory consumption of the computations also scale with the number of harmonics.

Theoretical results about the convergence of spectral methods (see *e.g.* Canuto *et al.* [9] for a comprehensive review) predict convergence of the numerical solution starting from a given number of harmonics, provided that the approximated function satisfies some regularity requirements [10]. Nevertheless, this number of harmonics is configuration-dependent and hardly predictable. In this work, we focus on the interface between two adjacent blade rows in a turbomachinery stage configuration, which involve flow across a series of fixed and rotating bladed wheels. Therefore, even though HB methods are capable to handle multistage configurations [6], this paper only focuses on rotor/stator or rotor/rotor stages. Studies on the convergence of Fourier-based time methods for turbomachinery simulations have been previously reported in the literature, but with scattered results. For instance, using a frequency-domain approach, Vilmin *et al.* [11] obtain accurate solutions using 5 harmonics for a compressor stage and 3 harmonics for a centripetal turbine stage. For a transonic compressor stage with forced blade vibration, Ekici *et al.* [12] use up to 7 harmonics with a time-domain harmonic balance approach. Finally, for a subsonic compressor stage, Sicot *et al.* [7] report that 4 harmonics is the minimal requirement to properly capture wake interactions as illustrated in Fig. 1.

The preceding examples show that no consensus exists in the literature concerning the number of harmonics needed to achieve convergence, even for similar configurations. The goal of the present paper is twofold: to analyze the convergence of Fourier-based time method, with focus on turbomachinery applications, and to provide a criterion for the minimal number of harmonics required to achieve a specified accuracy level.

(a) reference unsteady simulation   (b) HB $N = 2$ (c) HB $N = 3$

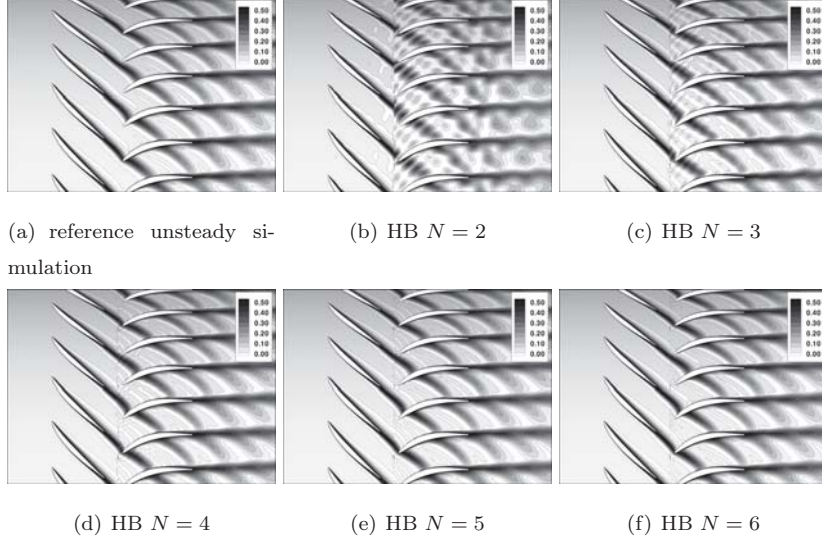(d) HB $N = 4$ (e) HB $N = 5$ (f) HB $N = 6$

Figure 1: Convergence of harmonic balance computations for a rotor/stator configuration from Sicot *et al.* [7].

The paper is organized as follows: first, we recall the design principles of the time-domain harmonic balance approach and theoretical results about the convergence of Fourier-based methods. Second, the HB method is applied to the linear advection equation supplemented with unsteady boundary conditions of different degrees of smoothness, to highlight the impact of solution regularity on HB convergence. Third, a model problem representative of a turbomachinery wake-passing configuration is set up, and different error measures are introduced to compare the numerical and analytical solutions. These error measures allows finally to define a prediction tool, which is applied to contra-rotating open rotor simulations.

2. Time-domain harmonic balance approach

2.1. Derivation for fluid dynamics applications

The Unsteady Reynolds-Averaged Navier-Stokes (U-RANS) equations are written in finite-volume semi-discrete form as:

$$V\frac{\partial W}{\partial t} + R(W) = 0, \tag{1}$$

with V the volume of the cell, R the residual resulting from the discretization of the fluxes and the source terms (including the turbulent equations), and W the average of the unknowns (conservative variables) over the control volume.

If the mean flow variables W are periodic in time with period $T = 2\pi/\omega$, so are the residuals $R(W)$ and the Fourier series of Eq. (1) is:

$$\sum_{k=-\infty}^{\infty} \left(ik\omega V\widehat{W}_k + \widehat{R}_k\right) e^{ik\omega t} = 0, \tag{2}$$

where $\widehat{W}_k$ and $\widehat{R}_k$ are the Fourier coefficients of W and $R(W)$, respectively, corresponding to the mode k:

$$W(t) = \sum_{k=-\infty}^{\infty} \widehat{W}_k e^{ik\omega t}, \quad R(t) = \sum_{k=-\infty}^{\infty} \widehat{R}_k e^{ik\omega t}. \tag{3}$$

The complex exponential family forming an orthogonal basis, the only way for Eq. (2) to be true is that the weight of every mode k is zero, which leads to an infinite number of steady equations in the frequency domain:

$$ik\omega V\widehat{W}_k + \widehat{R}_k = 0, \qquad \forall k \in \mathbb{Z}. \tag{4}$$

McMullen *et al.* [13, 14, 15] solve a subset of these equations up to mode N, $-N \le k \le N$, yielding the Non-Linear Frequency Domain (NLFD) method.

The principle of the time-domain Harmonic Balance (HB) approach [4], sometimes referred to as the Time Spectral Method (TSM) [5, 16], is to use an Inverse Discrete Fourier Transform (IDFT) to cast back this subset of $2N + 1$ frequency-domain equations into the time domain. The IDFT then induces linear relations between Fourier coefficients $\widehat{W}_k$ and a uniform sampling of W at

5

$2N + 1$ instants in the period:

$$W_n = \sum_{k=-N}^{N} \widehat{W}_k \exp(i\omega n\Delta t), \qquad 0 \le n < 2N + 1, \tag{5}$$

with $W_n \equiv W(n\Delta t)$ and $\Delta t = T/(2N + 1)$. This leads to a new system of $2N + 1$ mathematically steady equations coupled by a source term:

$$R(W_n) = -VD_t(W_n), \qquad 0 \le n < 2N + 1. \tag{6}$$

Equivalently, Eq. (6) may be rewritten as:

$$VD_t(W_n) + R(W_n) = 0, \qquad 0 \le n < 2N + 1. \tag{7}$$

By comparison of Eq. (7) and Eq. (1), it appears that the source term $VD_t(W_n)$ plays the role of a spectral approximation of the time derivative in Eq. (1). This new time operator connects all the time instants~~instances~~ and can be expressed analytically as:

$$D_t(W_n) = \sum_{m=-N}^{N} d_m W_{n+m}, \tag{8}$$

with:

$$d_m = \begin{cases} \frac{\pi}{T}(-1)^{m+1} \csc\left(\frac{\pi m}{2N+1}\right) & , m \ne 0, \\ 0 & , m = 0. \end{cases} \tag{9}$$

A similar derivation can be made for an even number of instants but Van der Weide *et al.* [17] proves that it can lead to a numerically unstable odd-even decoupling.

A pseudo-time (τ_n) derivative is added to Eq. (6) to march the equations in pseudo-time to the steady state solutions of all the instants:

$$V\frac{\partial W_n}{\partial \tau_n} + VD_t(W_n) + R(W_n) = 0, \qquad 0 \le n < 2N + 1. \tag{10}$$

2.2. Convergence of the spectral operator

The convergence of the spectral operator depends on the regularity of the approximated function. Consider a function $u(t)$ that is continuous, periodic and bounded in $[0, T]$ and let $P_N(u(t))$ denote its truncated Fourier series:

$$P_N(u(t)) = \sum_{k=-N}^{N} \widehat{u}_k e^{ik\omega t}. \tag{11}$$

The $\mathcal{L}_2$-norm of the error writes:

$$\|u\|_2 = \left(\int_0^T |u(t) - P_N(u(t))|^2 \, \mathrm{d}t \right)^{1/2}. \tag{12}$$

If $u(t)$ is m-times continuously differentiable in $[0, T]$ ($m \geq 1$) and its j-th derivative is periodic on $[0, T]$ for all $j \leq m - 2$ then, it exists $k_0 \in [1, N]$ such that for $k > k_0$:

$$\widehat{u}_k = \mathcal{O}(k^{-m}), \tag{13}$$

where $\widehat{u}_k$ is the k-th Fourier coefficient of $u(t)$. This equation means that, the more regular the function is, the faster the convergence rate of the Fourier coefficients. The property of the error to decay exponentially as soon as the function is approximated by a number of harmonics greater than k_0 is called spectral accuracy [9]. Note that k_0 is not known but is rather essential for the analysis. For k below k_0, approximating the function $u(t)$ with its Fourier series yields unacceptably high errors.

2.3. ~~Motivating example: numerical derivation of a smooth function~~

3. Linear advection of a periodic perturbation

To properly assess the convergence of the spectral operator and thus the HB computations, a model problem is set up. We consider the linear advection equation:

$$\frac{\partial u}{\partial t} + c \frac{\partial u}{\partial x} = 0, \tag{14}$$

with the constant advection speed c assumed to be positive. The equation is solved in the domain $[0, 1]$. Periodic perturbations of different shapes (and therefore, different smoothness) are imposed at the left boundary:

$$u(0, t) = u_l(t), \tag{15}$$

where u_l is a periodic function of period $T = 1/c$. These perturbations are advected across the computational domain and leave through the right boundary. After a transient of time length $T_{trans} = 1/c$, the solution at any point x in

7

the space domain achieves a periodic state. The exact solution for this periodic state is a periodic function of the form:

$$u_{ex}(x, t) = u_l(t - x/c)\underline{u_l(x/c + t)}.$$ (16)

The space derivative is discretized by means of a centered fourth-order finite-difference scheme on an uniform fine Cartesian mesh ($\Delta x = 0.002$). According to the theory of characteristics, the solution at the last mesh point on the right of the domain cannot be imposed and is thus extrapolated from the inside, for the last two points. Time-discretization is achieved through the HB method described in Sec. 2.

A standard four-step Runge-Kutta method [18] is used to pseudo-time march the HB equations to the steady state. The CFL number in pseudo-time is set to 1 to ensure stability of the explicit time-marching scheme.

To compare numerical and exact solutions, the discrete $\mathcal{L}_2$-norm of the error in time is computed over all the time instants~~instances~~ at each grid points over the domain. Then, the average in space is computed.

In the following, we consider solutions of the preceding problem for different choices of the left boundary condition.

3.1. Sum of sine functions

First of all, a finite sum of sine functions~~, similar as the one used in Sec. ??,~~ is applied at the left boundary:

$$u_l(t) = \cos(\omega t) + \sin(2\omega t) + \cos(3\omega t) + \sin(4\omega t) + \cos(5\omega t).$$ (17)

Harmonic balance computations are run with 1 to 10 harmonics. For each computation ranging from $N = 1$ to $N = 6$, we show spatial distributions of the solution at three time instants~~instances~~, namely $t = 0$, $t = T/3$ and $t = 2T/3$. Since these instants~~instances~~ are not necessarily used in the HB discretization, a temporal interpolation is performed. To do so, the frequency content of the HB solution is used together with an inverse Fourier transform on the time-vector $[0, T/3, 2T/3]$. Figure 2 depicts the results of HB computations using 1 to 6 harmonics. The analytical solution is also reported for comparison.
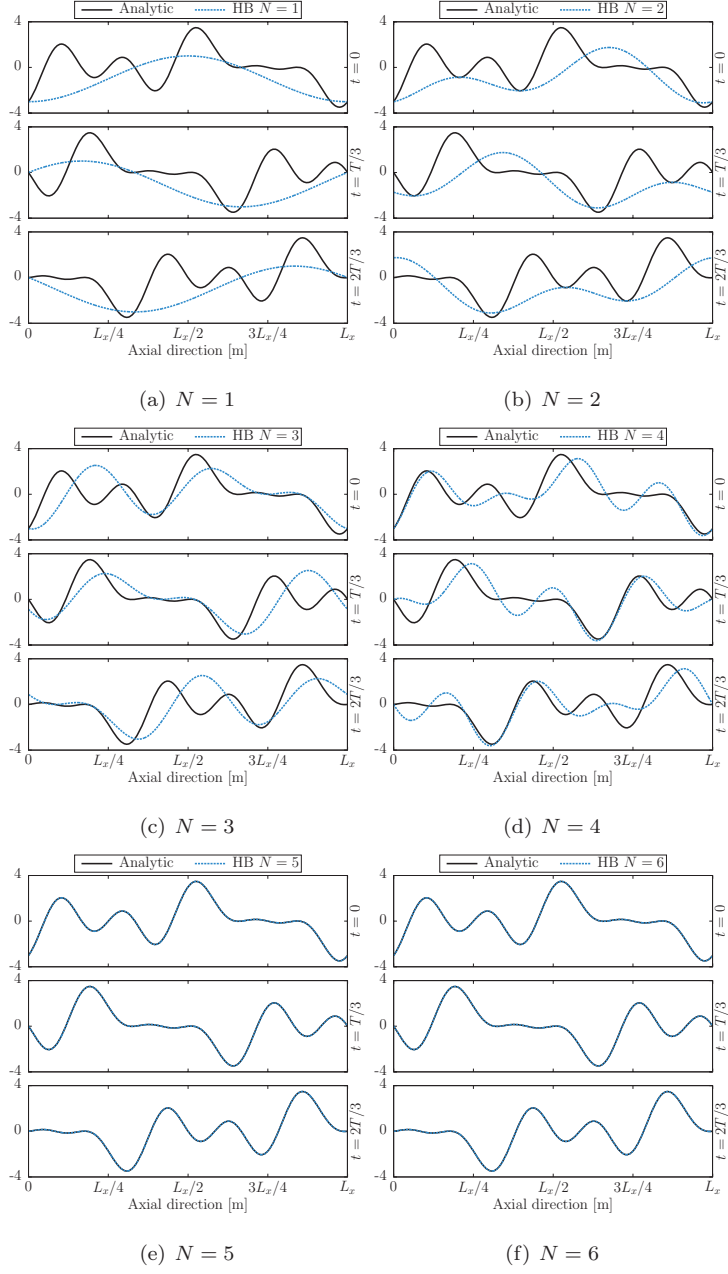
8

Figure 2: Linear advection of a sum of sine functions: numerical solutions at different time instants~~instances~~ for different numbers of harmonics.

9

The accuracy of the solution improves with the number of harmonics, until it reaches the frequency content of the injected signal, i.e. 5 harmonics. For higher sampling levels, the results of HB computations are superimposed with the analytical solution.

The $\mathcal{L}_2$-norm of the relative error as a function of the number of harmonics is shown in Fig. 3. Two results are displayed: one for the reference mesh (2,000 grid points) and one for a refined mesh (4,000 grid points). The convergence
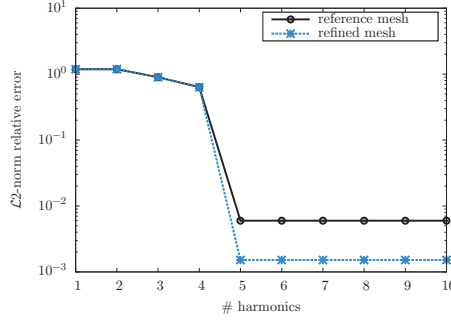

Figure 3: Linear advection of a sum of sine functions: convergence of the HB method error.

of the HB computations is slow for $N \leq 4$. However, when the number of harmonics composing the injected function is reached ($N = 5$), the error is minimum and computing more harmonics does not change the error. It seems that the convergence rate of Fourier-based time methods is inherently linked to the spectrum of the temporal phenomenon that one wants to capture. Here a finite discrete spectrum composed of only five harmonics is imposed. The value of the plateau obtained after $N = 5$ is representative of the error introduced by the different discretizations. In fact, refining the mesh changes this value without modifying the error levels of the lower harmonics points. Note that the error is the true residual, meaning that the computation is compared to the analytical result. This is why the only way to have a zero machine value~~like in Fig. ??,~~ would be to have an infinite number of grid points and pseudo-iterations.

The temporal discrete Fourier transform of the computational results is compared to the analytical results in Fig. 4. When the number of harmonics grows
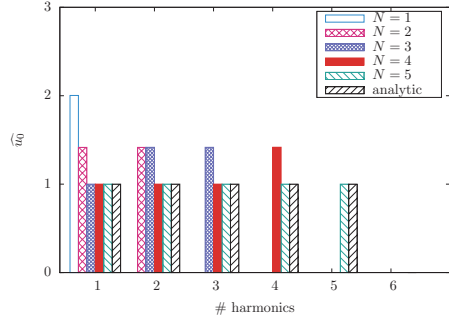
10

Figure 4: Linear advection of a sum of sine functions: discrete Fourier transform.

in the spectral computations, the Fourier transform gets closer to the analytical solution. When the HB solution contains the whole frequency content of the injected function, the numerical results are superimposed with the analytical ones. For intermediate sampling frequencies, as for instance the three-harmonics HB computation, the resolved harmonics have higher amplitudes than the exact one, since they compensate for harmonics that are not resolved.

When the number of harmonics composing the spectrum of the computed signal is reached, the computational results are superposed with the analytical ones with plotting accuracy, namely we obtain spectral accuracy.

3.2. ~~Rectangular function~~

3.3. Toward turbomachinery wakes

Consider for simplicity a turbomachinery stage composed of two rotors. A wake is shed behind the upstream and the downstream rotor. It is stationary in the frame of reference attached to the upstream wheel. However, when it crosses the rotor-rotor interface, the wake becomes unsteady in the frame of reference of the second wheel. Thus, an upstream steady spatial distortion becomes unsteady in the downstream row.

Lakshminarayana and Davino [19] showed that the wake behind turbomachinery blade follows a similarity law for the velocity. It can be empirically
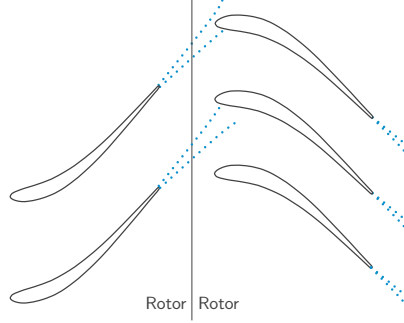
Figure 5: Characteristic rotor-rotor configuration of a turbomachinery. Dotted lines depict wakes.

approximated by a Gaussian function:

$$u(\theta) = u_m - \Delta u \cdot e^{-0.693\left(2\frac{\theta}{L}\right)^2}, \tag{18}$$

where u_m denotes the free-stream velocity, Δu the axial wake velocity deficit, θ the azimuthal coordinate and L the wake width, defined as the full width at half maximum.

Thus, in the downstream reference frame, wakes coming from the upstream wheel can be represented, to a first approximation, as the periodic advection of a Gaussian function from the inter-wheel interface.

We consider again the linear advection problem, with u_l now taken equal to a Gaussian function of the form Eq. (18). The width L is set to 10% of the domain size, u_m is set to c and Δu to 10% of u_m.

Figure 6 depicts the HB computations for one to six harmonics. The numerical solution convergences toward the exact Gaussian function when increasing the number of harmonics~~starting from $N = 6$ harmonics~~. When this number~~the number of harmonics~~ is too small, the width and the depth of the wake are badly approximated by the method, and the solution exhibits some spurious oscillations.

Figure 7 shows the quantitative convergence of the $\mathcal{L}_2$-norm of the relative error~~error~~. The convergence curves for the previous~~two~~ function ~~studied in the previous sections~~ is~~are~~ also reported for comparison. The error follows now a

12

(a) $N = 1$

(b) $N = 2$

(c) $N = 3$

(d) $N = 4$

(e) $N = 5$

(f) $N = 6$
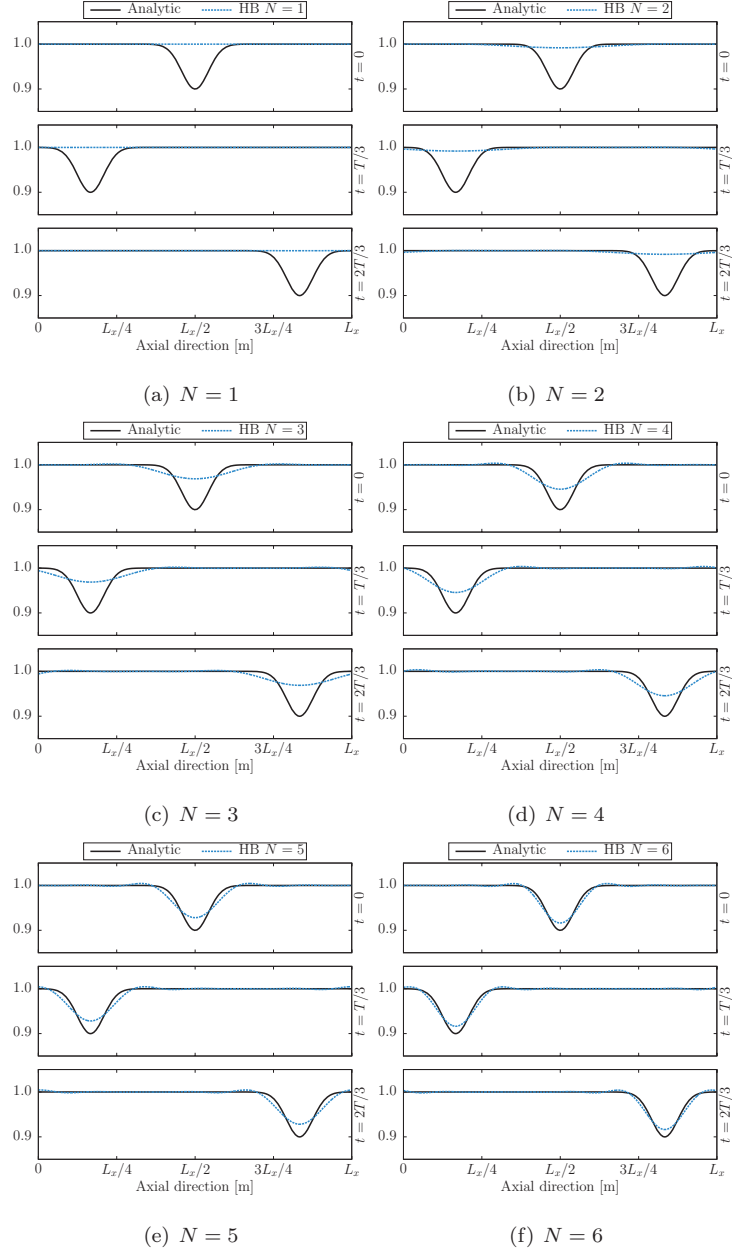
Figure 6: Linear advection of a Gaussian function representing a turbomachinery wake: numerical solutions at different time instants~~instances~~ for different numbers of harmonics.
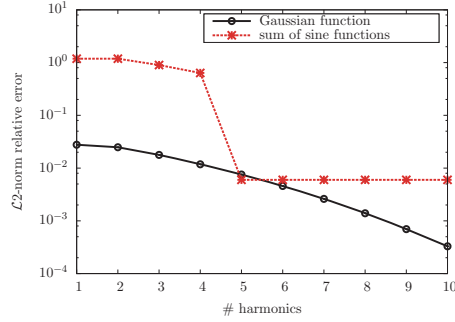
13

Figure 7: Linear advection of a Gaussian function representing a turbomachinery wake: convergence of the HB method error.
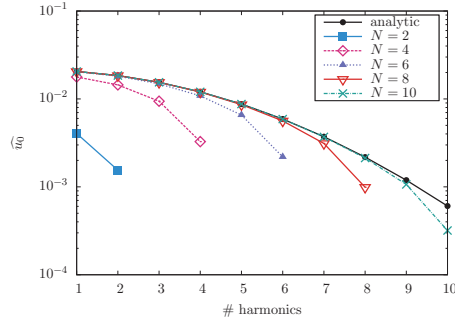
nearly exponential convergence.

Figure 8: Linear advection of a Gaussian function representing a turbomachinery wake: discrete Fourier transform.

The discrete Fourier transform of the results is depicted against the analytical result in Fig. 8. The $N = 2$ and $N = 4$ computations badly capture the amplitudes of the resolved harmonics. Starting from $N = 6$, some of the lower frequencies are correctly captured, whereas high frequencies are always under-estimated. This improves when further harmonics are added to the computation.

For a better understanding of the HB convergence behavior, we consider the spectral content of the Gaussian wake model. Precisely, the Fourier transform

14

$\widehat{g}$ of a Gaussian function g defined as:

$$g(x) = Ae^{-\alpha x^2}, \tag{19}$$

where A and α are constants, is:

$$\widehat{g}(f) = A'e^{-\alpha' f^2}, \tag{20}$$

where:

$$\begin{cases} A' = A\sqrt{\frac{\pi}{\alpha}}, \\ \alpha' = \frac{\pi^2}{\alpha}. \end{cases} \tag{21}$$

For the similarity law of Lakshminarayana and Davino, α and α' can be identified as:

$$\alpha = 0.693 \left(\frac{2}{L}\right)^2, \quad \alpha' = \frac{1}{0.693}\left(\frac{\pi L}{2}\right)^2. \tag{22}$$

The exponential factor of the wake law α is inversely proportional to its Fourier counter-part α', meaning that their width will vary in opposite way: the thinner the wake, the wider its spectrum and *vice-versa*~~vice-versa~~.

The convergence rate is inherently linked to the spectrum of the considered unsteady signal. As for the present case we know the analytical wake spectrum, we define the theoretical truncation error as the ratio of the energy contained in the unresolved part of the spectrum to the overall energy content of the full spectrum:

$$\varepsilon_{th}(f) = \sqrt{\frac{\int_f^\infty |\widehat{g}(\zeta)|^2\,\mathrm{d}\zeta}{\int_0^\infty |\widehat{g}(\zeta)|^2\,\mathrm{d}\zeta}}. \tag{23}$$

Introducing the error function defined as:

$$\mathrm{erf}(x) = \frac{2}{\sqrt{\pi}}\int_0^x e^{-t^2}\,\mathrm{d}t, \tag{24}$$

and the complementary error function defined as:

$$\mathrm{erfc}(x) = 1 - \mathrm{erf}(x), \tag{25}$$

then:

$$\int_0^\infty |\widehat{g}(\zeta)|^2\,\mathrm{d}\zeta = \frac{1}{2}\int_{-\infty}^\infty |\widehat{g}(\zeta)|^2\,\mathrm{d}\zeta \tag{26}$$

$$= \frac{A'^2}{2}\sqrt{\frac{\pi}{2\alpha'}}, \tag{27}$$

15

and:

$$\int_f^\infty |\widehat{g}(\zeta)|^2 \, \mathrm{d}\zeta = \frac{A'^2}{2}\sqrt{\frac{\pi}{2\alpha'}}\,\mathrm{erfc}(\sqrt{2\alpha'}f). \tag{28}$$

The theoretical truncation error can then be written as:

$$\varepsilon_{th}(f,L) = \sqrt{\mathrm{erfc}(\sqrt{2\alpha'(L)}f)}. \tag{29}$$

One can notice from Eq. (29) that the truncation error does not depend on the wake deficit Δu but only on the wake width L.
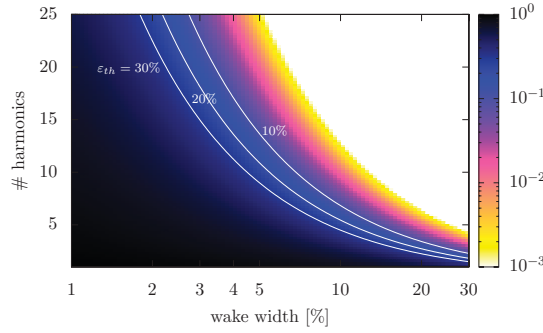

Figure 9: Theoretical truncation error of the Lakshminarayana and Davino wake law.

Eq. (29) is depicted in Fig. 9. It can be seen that the wider the spectrum, the higher the number of harmonics needed to reach a certain level of error. Moreover, for a thin wake width (*e.g.* ~~e.g.~~ 2% of the pitch) the number of harmonics required to capture it with a truncation error of 10% is up to 25 harmonics. In the limit of $L \to 0$, the wake becomes a Dirac function which represents the worst possible case. In the preceding example, the Gaussian function had a width of 10% which, according to Eq. (29), is captured by using $N = 7$ harmonics for a 10% error target.

4. Application to a model turbomachinery configuration

4.1. Extension of the harmonic balance approach to turbomachinery computations

To efficiently apply the HB approach to turbomachinery configurations, phase-lag boundary conditions [20] are used to cut down the mesh size by using

a grid that spans only one blade passage per row. The phase-lag boundary conditions are two-fold: i) the azimuthal boundaries of a passage and ii) the blade row interface which must handle different row pitches on either sides (Fig. 10). Furthermore, in the HB framework, each row captures the blade passing frequency of the opposite row leading to different time samples solved in each row.

Phase-lag boundary conditions only account for deterministic row interactions, and therefore can not model natural unsteady phenomenon, such as vortex shedding for instance. Actually, the phase-lag condition is based on the space-time periodicity of the flow variables. It states that the flow in one passage θ is the same as the next passage $\theta + \Delta\theta$ but at another time $t + \delta t$:

$$W\left(\theta + \Delta\theta, t\right) = W\left(\theta, t + \delta t\right), \tag{30}$$

where $\Delta\theta$ is the pitch of the considered row. The time lag δt can be expressed as the phase of a rotating wave traveling at the same speed as the relative rotation speed of the opposite row: $\delta t = \beta/\omega_\beta$. The Inter-Blade Phase Angle β (IBPA) depends on each row blade count and relative rotation speed. It is analytically given by Gerolymos and Chapin [21]. The Fourier transform of Eq. (30) implies that the spectrum of the flow in a passage is equal to the spectrum of the neighbor passage modulated by a complex exponential depending on the IBPA:

$$\widehat{W}_k(x, r, \theta + \theta_G) = \widehat{W}_k(x, r, \theta)e^{ik\beta}.$$

At the azimuthal boundaries, this modulation can be computed on the fly in the HB framework as a sampling of the time period is always known and it is straightforward to derive an analytic derivation in the time domain (see Ref. [7]). The blade row interface is more complex as the different pitches and relative motion of the rows require to duplicate the flow in the azimuthal direction using the phase-lag periodicity. A time interpolation also occurs to take the different time samples into account and a non-abutting mesh technique is applied as the mesh will unlikely have matching cells. To remove spurious waves, an over-sampling followed by a filtering are performed.
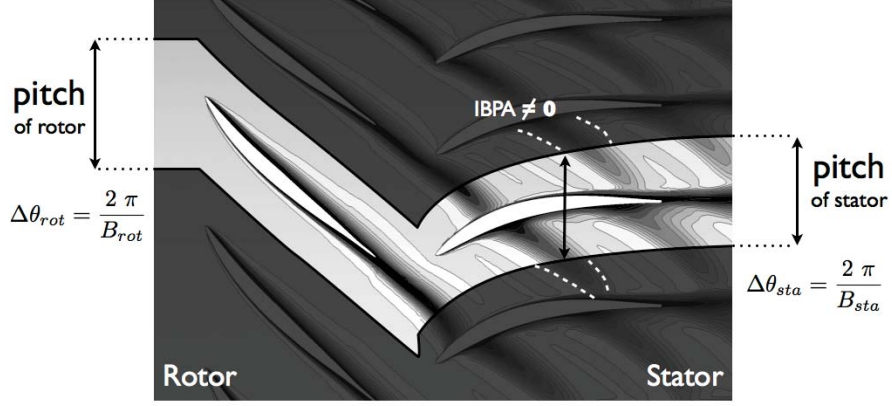
17

Figure 10: Definition of pitches and IBPA used with phase-lag boundary conditions.

The time-domain harmonic balance method has been implemented by CER-FACS in the *elsA* solver [22] developed by ONERA. This code solves the RANS equations using a cell-centered approach on multi-blocks structured meshes. Using the HB method, significant savings in CPU cost have been observed in applications such as rotor/stator interactions [7] and dynamic derivatives computation [23].

4.2. Numerical Setup

We consider a simplified configuration modeling a turbomachinery stage. The configuration consists of a spatially periodic azimuthal perturbation advected downstream of the inlet boundary of the computational domain. The domain is made of two grid blocks in relative motion so that the perturbation, which is steady in the upstream block, is seen as unsteady by the downstream one. It~~, and~~ is thus representative of turbomachinery wakes advected across an inter-wheel interface. The blocks are generated in cylindrical coordinates such that the presented configuration can be assimilated to a slice of a turbomachinery stage. Without loss of generality, we set the rotation velocity of the upstream block to zero (stator). The stator is composed of $B_{stator} = 10$ "virtual" blades and the rotor by $B_{rotor} = 12$ "virtual" blades. These are termed

18

virtual blades as no blade is actually meshed. The pitch ratio is representative of contra-rotating open rotor applications in which the first row contains more blades than the second (see Sec. 5). Indeed, in these applications, the number of blades is typically smaller than classical turbomachinery configurations.

A wake is axially injected at the inlet of the stator block following the Lakshminarayana and Davino similarity law defined in Eq. (18). It is schematically represented in Fig. 11. This is thus a representative model problem of the wake shed by an upstream row that crosses the rows interface, here the stator-rotor interface.

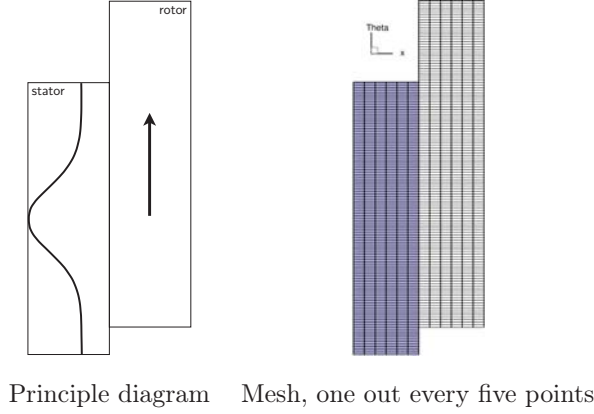Principle diagram   Mesh, one out every five points

Figure 11: Model turbomachinery configuration.

The flow is modeled through the Euler equations in order to avoid wake thickening associated with viscous effects. The velocity is not imposed at the inlet directly but rather through the total pressure and total enthalpy distributions:

$$p_{i0}(\theta) = p_{i_{ref}} \left[1 - \Delta p_i \cdot e^{-0.693\left(2\frac{\theta}{L}\right)^2} \right],　\tag{31}$$

$$h_{i0}(\theta) = h_{i_{ref}} \left[1 - \Delta h_i \cdot e^{-0.693\left(2\frac{\theta}{L}\right)^2} \right],　\tag{32}$$

where p_{i0} is the inlet total pressure, Δp_i the total pressure deficit in the wake, h_{i0} the inlet total enthalpy, Δh_i the total enthalpy deficit in the wake and L the wake width. To impose a realistic distortion, the total pressure and enthalpy deficits are estimated from a separate turbomachinery simulation. This leads

19

to $\Delta p_i = 0.025$ and $\Delta h_i = -0.007$. The negative sign is due to overturning in the wake, which is due to velocity composition, and therefore specific to rotors. The static pressure p_{s_1} is imposed at the outlet:

$$p_{s_1} = \frac{p_{ref}}{\left(1 + \frac{\gamma-1}{2} M_{ref}^2\right)^{\frac{\gamma}{\gamma-1}}}. \tag{33}$$

Thethe mean velocity is thus set by imposing the target mean Mach number value M_{ref}. At the azimuthal boundaries, phase-lag conditions [20] are used to take into account for the space-time periodicity.

Roe's scheme [24] along with a second-order MUSCL extrapolation is used for the spatial discretization of the convective fluxes. An, and implicit backward Euler scheme is used to march the HB equations in pseudo-time.

A parametric study is carried out over the two parameters that influence the truncation error as defined in Eq. (23): the number of harmonics and the wake width. The number of harmonics used for the computations ranges from 1 to 25. The wake width L, that drives Eq. (31) and (32) varies between 1% and 30% according to a logarithmic scale to ease the visualization of the results.: 375 computations are performed in total.

Each grid block has a radial extent of five grid points (*i.e.* four cells). The azimuthal grid density in the stator and rotor blocks is kept similar to guarantee a consistent capture of the wake on each side of the interface. To do so, if $\Delta\theta_{cell}$ denotes the azimuthal length of a cell at the interface, then:

$$\Delta\theta_{cell} = \frac{2\pi}{B_{stator}} \frac{1}{N_{stator}} = \frac{2\pi}{B_{rotor}} \frac{1}{N_{rotor}}, \tag{34}$$

where N_{stator} and N_{rotor} are the number of cells in the stator and the rotor, respectively.

Mesh convergence for the thinnest wake (1% of the pitch) is obtained with 500 cells in the azimuthal direction of the stator which gives 600 cells for the rotor block. 30 grid points are put in the axial direction. Moreover, a constant aspect ratio of 5 with respect to the azimuthal length of the cells is kept, which sets the axial length of the case. This leads to a total number of grid points of

20

approximately 170,000. Note that the memory requirement of an HB simulation is $2N + 1$ times that of the equivalent steady case. An equivalent steady computation to $N = 25$ would thus require $(2 \times 25 + 1) \times 170,000 = 8,670,000$ grid point mesh. The grid used for the computations is shown in Fig. 11.

Convergence of the iterative procedure used to solve the HB equations is achieved after 3,000 iterations ~~for all the simulations,~~ as presented in Fig. 12. More than a three order of magnitude decrease is reached for all the simulations. Small discrepancies are observed on the residual convergence for different wake thicknesses while the number of harmonics does not influence the convergence (Fig. 12(a)).
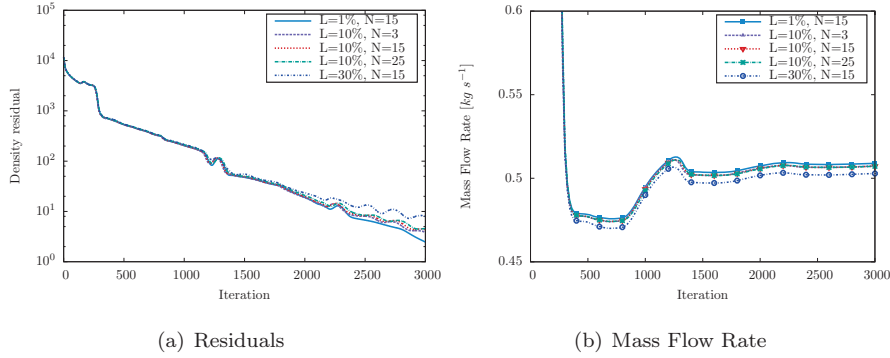

(a) Residuals　　　　　　(b) Mass Flow Rate

Figure 12: Convergence of the turbomachinery stage computations.

4.3. Spectral convergence study

The primary interest in this section is the wake capturing capabilities of the Fourier-based time method in the rotating part. To analyze this, two error measures are defined and evaluated.

Those measures address the loss of information introduced by the HB approach at the interface. This loss is firstly evaluated by analyzing the spectrum from a purely spatial point of view. Then, an hybrid spatial/temporal point of view is taken. This finally allows to assess the filtering introduced by the harmonic balance method on both the time and spatial signals.

21

In fact, in the stator part, the wake is steady and is thus not filtered by the HB operator. Conversely, in the rotor part, the steady wake becomes unsteady due to the relative speed difference between the stator and the rotor. However, only a finite number of harmonics N is used to describe the unsteady field, hence the filtering.

4.3.1. Spatial-spectrum based error measure

Initially, we propose an error measure (ε_1) based on the loss of signal energy induced by the harmonic method at the interface. In fact, in the stator part, the wake is steady and is thus not filtered by the HB operator. Conversely, in the rotor part, the steady wake becomes unsteady due to the relative speed difference between the stator and the rotor. However, only a finite number of harmonics N is used to describe the unsteady field, hence the filtering.

The first error quantification ε_1 is set up to quantify this filtering by using only spatial information and is defined as the $\mathcal{L}_2$-norm applied on the difference between the rotor and the stator spectra. It is equivalent to the analytical truncation error defined in Eq. (23). Indeed, the error is defined as the ratio of the unresolved energy in the rotor block to the energy of the full spectrum, *i.e.* that of the stator block:

$$\varepsilon_1(N) = \sqrt{\frac{\sum_{f=1}^{f_{max}} |\widehat{s}_N^{\theta}(f) - \widehat{r}_N^{\theta}(f)|^2}{\sum_{f=1}^{f_{max}} |\widehat{s}_N^{\theta}(f)|^2}}, \tag{35}$$

where $\widehat{s}_N^{\theta}$ denotes the spatial Fourier transform (indicated by the $\widehat{\cdot}$ operator) of the azimuthal extraction (shown by superscript θ) of the result of a HB simulation using N harmonics, in the stator; $\widehat{r}$ denotes the spectrum of the signal transferred to the rotor. The highesthigher frequency present in the spectrum is dictated by the spatial discretization. Thus, $f_{max} = 1/2\Delta\theta_{cells}$, using the notations of Eq. (34). As the azimuthal cell size is similar in both blocks, the same sampling is used leading to the same frequencies in both stator and rotor spectra. Details of the algorithm used to compute ε_1 are given in Appendix A.

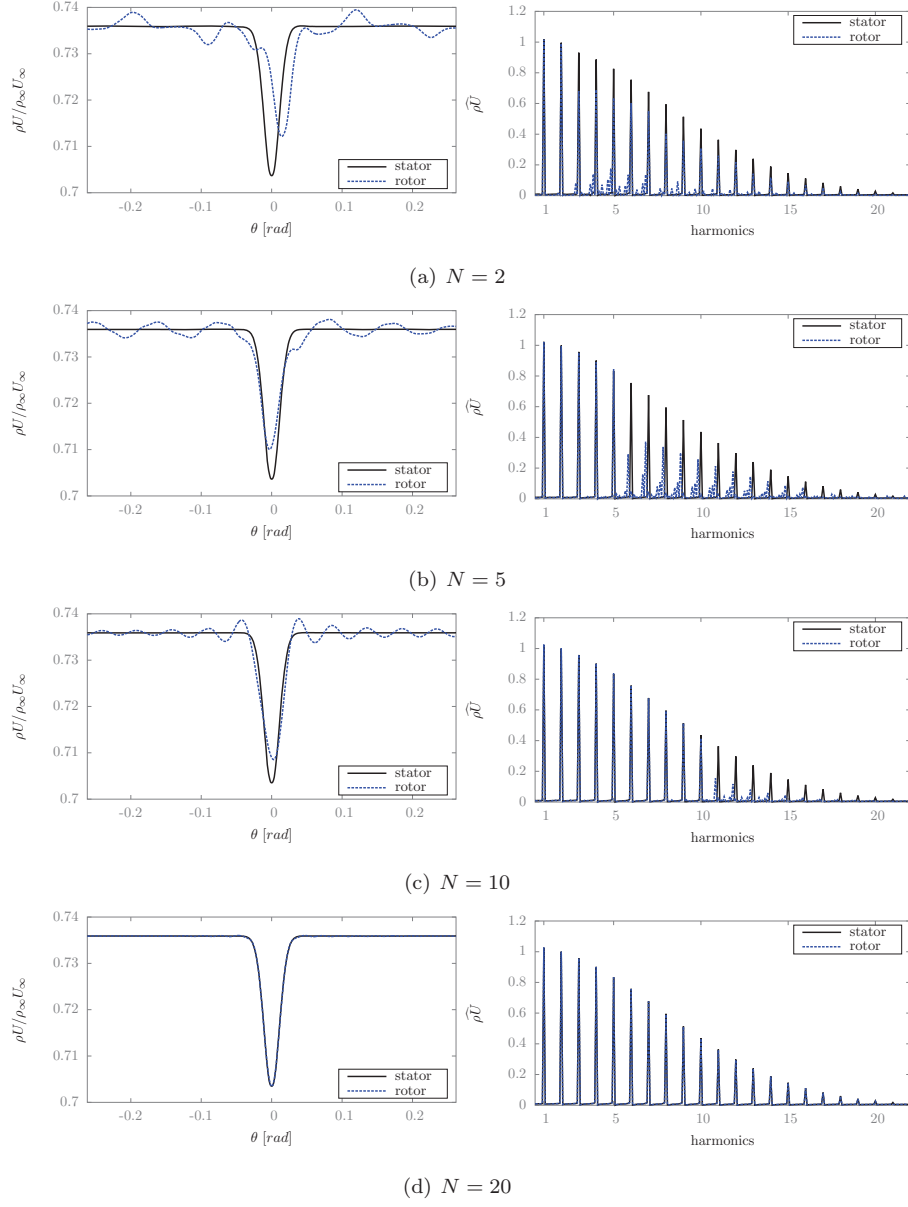(a) $N = 2$

(b) $N = 5$

(c) $N = 10$

(d) $N = 20$

Figure 13: Wake of $L = 5\%$ width extracted in stator and rotor blocks. Signal and spatial Fourier analysis for different computations.

The azimuthal velocity distributions (left hand-side) and the corresponding spatial spectra (right hand-side) are presented in Fig. 13 for a relative wake thickness of 5% with respect to the pitch and for HB computations using $N = 2$, 5, 10 and 20, respectively. For the stator, the azimuthal distribution follows a Gaussian function as expected. On the contrary, the rotor distribution is aliased by the HB discretization and exhibits spurious oscillations that tend to disappear when the number of harmonics used in the computation increases. For $N = 10$, some oscillations are still present, but the wake captured in the moving block begins to converge to that leaving the upstream block.

The filtering introduced by the HB approach acts primarily on the time resolution. For under-resolved HB computations, a dissipation error is observed. This dissipation is not spatially uniform and gives rise to dispersion errors on the spatial spectrum and to spurious high-frequencies as shown in Fig. 13. These effects vanish when the HB computations converge *i.e.* for $N \geq 10$. This explains why~~Therefore,~~ the spectrum of the unresolved spurious frequencies is imposed to have a zero amplitude value to compute ε_1.

Inspection of the spectra suggests the same conclusions. The amplitude of $\widehat{\rho U}$ improves when increasing the number of harmonics. As previously mentioned, for under-resolved HB computations, a dispersion error is introduced and spurious high-frequencies appear in the spatial spectra as shown in Fig. 13 for $N = 2$ to $N = 10$. For $N = 20$, the spectrum of the rotor block matches that of the stator block. This is consistent with the theoretical analysis, in which more than $N = 10$ harmonics are needed to capture the wake with less than 20% of error for this particular wake width (see Fig. 9).

In summary, for this wake thickness, the temporal filtering on a simulation involving less than ten harmonics is too harsh and leads to a significant amount of unresolved energy, which deteriorates the numerical representation of the wake.

For a more quantitative analysis, we compute the error measure ε_1 for each computation ranging over different wake thicknesses and numbers of harmonics. Figure 14 summarizes the results~~results~~. Because it quantifies the unresolved
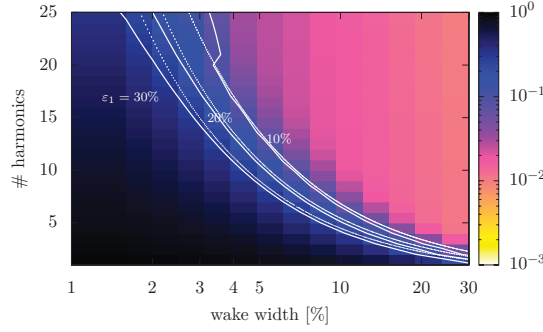
Figure 14: Evaluation of the error due to the wake capturing using the first error quantification ε_1, and comparison with analytical error (dotted lines).

energy in comparison to the resolved energy, ε_1 exhibits a behavior similar to that of the theoretical error ε_{th} for a Gaussian function (Fig. 9). The iso-error contours have a similar shape as the analytical ones. The conclusions are equivalent: the truncation error decreases with the wake thickness and with the number of harmonics used to capture the wake. Nevertheless, for thicker wakes and higher numbers of harmonics, the error measure ε_1 is over-estimated. For instance, around $N = 15$ and for $L = 25\%$, $\varepsilon_1 \approx 10^{-2}$ whereas the theoretical error ε_{th} is less than 10^{-4}. The error measure ε_1 does not represent a realistic measure, because of the spatial Fourier transform performed to compute the error, as discussed in the following. As shown in Fig. 15, the Fourier transform of the spatial signal in the stator block tends to a plateau. The thicker the wake, the lower the frequency for which the plateau appears: approximately 15 harmonics for $L = 10\%$ (see Fig. 15(a)) and 6 harmonics for $L = 25\%$ (see Fig. 15(b)). Actually, for a N-harmonic HB computation, the spectrum is explicitly filtered in the moving block leading to an amplitude equal to zero above the Nth harmonic. Therefore, when the HB computations are converged, the difference between the spatial spectra in the stator and in the rotor block is driven by the plateau present in the spatial spectrum of the stator block.

In fact, this behavior is linked to the windowing of the signal on a bounded interval, the pitch. To highlight that, the influence of a modification on the
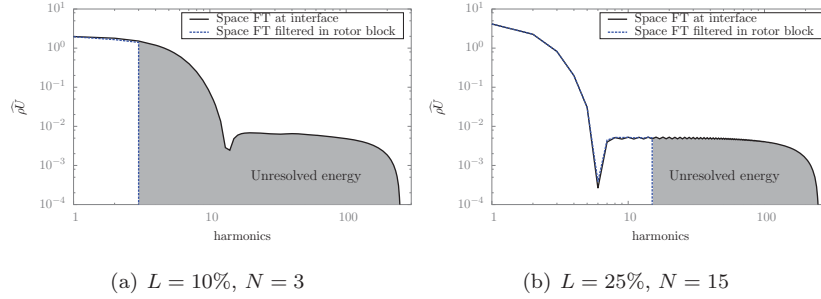
(a) $L = 10\%$, $N = 3$ (b) $L = 25\%$, $N = 15$

Figure 15: Discrepancies between the spectrum at the interface and in the rotor block, for varying wake widths and number of harmonics.spatial and temporal spectra.

inlet boundary condition is analyzed. The inlet wake distortion used in the model turbomachinery configuration is originally based on the analytical Lakshminarayana and Davino Gaussian law (see Eq. (18)). However, this law is discretized and imposed on a bounded interval that spans the angular pitch. As the relative thickness increases, the inlet condition diverges from the analytical Gaussian law for which the angular pitch is theoretically infinite. This is shown in Fig. 16 through the spectra of three Gaussian laws. The relative thickness of the laws are modified through the size of the pitch $\Delta\theta$. The multiplication by a factor 100 of the pitch leads to a disappearance of the plateau in the spectrum, which accurately matches with the Fourier transform of a Gaussian function.

To sum up, a plateau appears in the spatial spectrum of the stator block. This plateau is explicitly filtered in the rotor block above the Nth harmonic, leading to an over-estimation of the first error measure. This over-estimation drives the error value for higher number of harmonics and thicker wakes.

4.3.2. Spatial/Time duality error measure

To get a more realistic error measure, we take again into account the energy loss through the interface, but based on a spatial/time duality. As this loss of energy is precisely related to the filtering introduced on the temporal signal by the HB approach, the second error quantification ε_2 addresses the result on the temporal information.

(a) Inlet $\Delta\theta = L$ (b) Inlet Spectrum $\Delta\theta = L$

(c) Inlet $\Delta\theta = 10L$ (d) Inlet Spectrum $\Delta\theta = 10L$

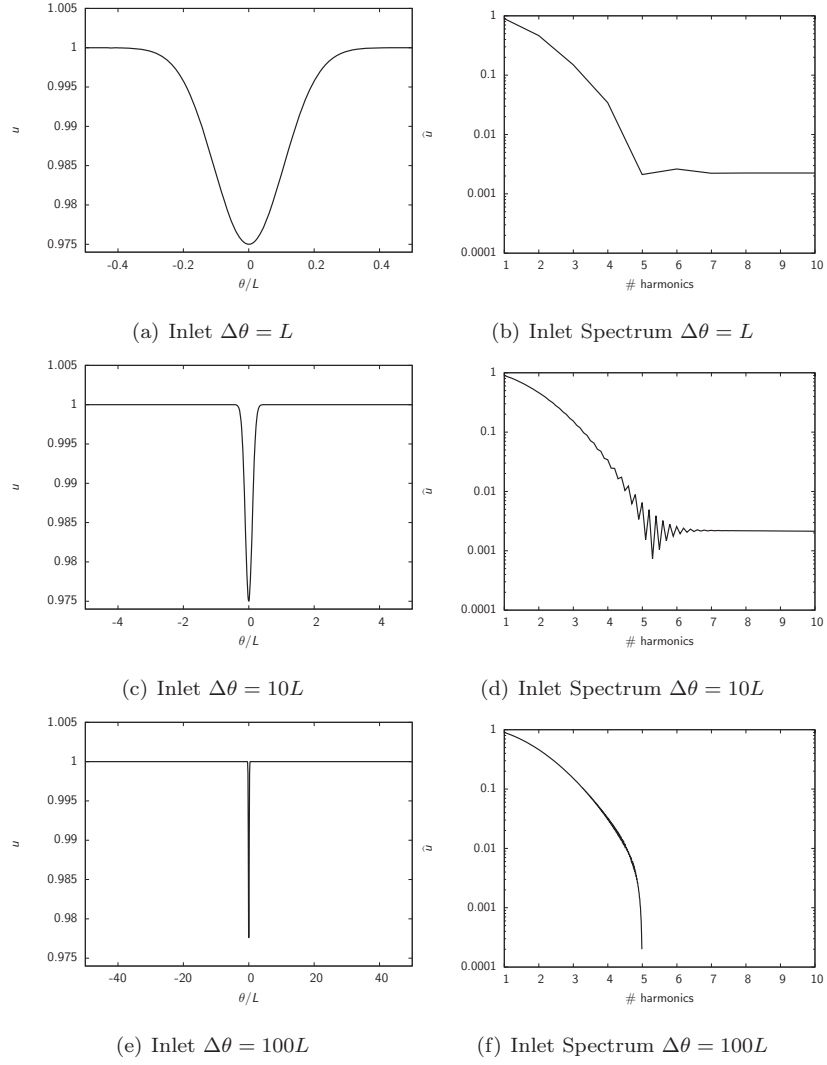(e) Inlet $\Delta\theta = 100L$ (f) Inlet Spectrum $\Delta\theta = 100L$

Figure 16: Evolution of the spectrum of the inlet boundary condition for different angular pitch.

Near the interface of the blocks, consider a fixed observer in the rotor frame of reference. This observer sees an unsteady wake passing as the blocks have a relative speed difference. The first error quantification has shown the influence of the number of harmonics on the spatial signal in the rotor block. The error quantification will now point that this spatial influence is due to a temporal filtering done by the HB approach.

Following the same notation as in Eq. (35), the second error measure is written as:

$$\varepsilon_2(N) = \sqrt{\frac{\sum_{f=1}^{f_{max}} |\widehat{s}_N^{\,\theta}(f) - \widehat{r}_N^{\,t}(f)|^2}{\sum_{f=1}^{f_{max}} |\widehat{s}_N^{\,\theta}(f)|^2}}, \tag{36}$$

where superscript t denotes the temporal version of the Fourier transform. By definition, ε_2 quantifies the matching between a spatial signal and a temporal information. Again, the error is described as the unresolved energy in the rotor block, divided by the energy of the full spectrum, $e.g.$ that of the stator block. For ε_1, the amplitude of the harmonics above the Nth one was imposed to zero. On the contrary, for ε_2, the temporal spectrum in the rotor block is by essence null above the Nth harmonic, as the filtering acts on temporal values. Details of the algorithm used to compute ε_2 are given in Appendix B.

Figure 17 shows time signals extracted at two different azimuthal positions at the interface of the rotor block, named loc 1 and loc 2. The small phase lag between the two signals is due to the space shift between the two points, and is the same for any choice of the number of harmonics used in the computation. On the contrary, differences in terms of amplitude are only due to the use of an insufficient number of harmonics: as the number of modes used for the time approximation is increased from $N = 5$ to $N = 15$, the amplitude of the space-shifted signals tends to converge to the same value, and spurious oscillations tend to disappear. Therefore, in the following, only loc 1 will be considered.

Figure 18 describes the space and time spectra of the axial momentum ρU at loc 1, for computations using $N = 2$, 5, 10 and 20 harmonics and for a wake width of $L = 5\%$. The spatial spectrum contains the whole wavelength content associated to the incoming wake; on the contrary, due to the filtering introduced
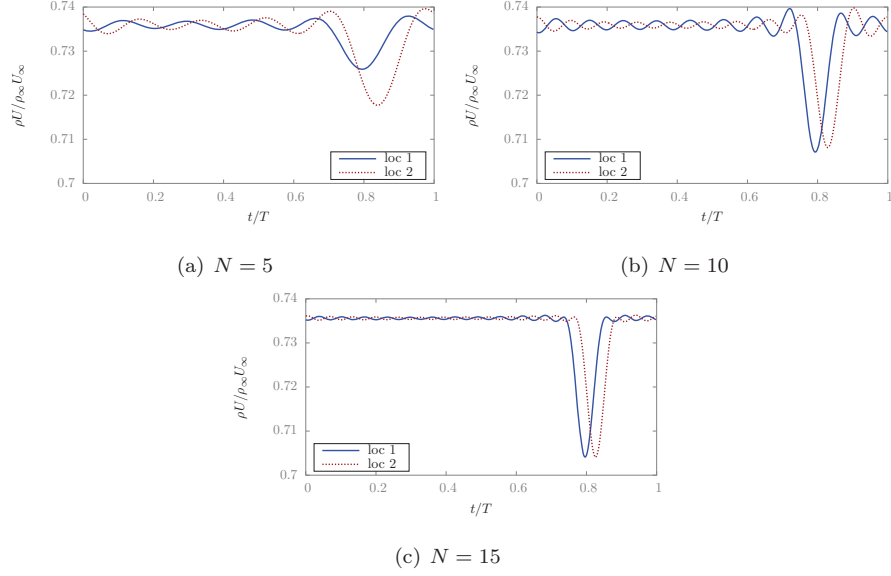
(a) $N = 5$ (b) $N = 10$

(c) $N = 15$

Figure 17: Temporal signal seen at loc 1 and loc 2 for a $L = 5\%$ wake width.

by the HB approach, the time spectrum is composed of only N harmonics. For computations using less than 10 time harmonics, time spectra are truncated, and the amplitude of ρU differs from that of the corresponding mode in the spatial spectrum. As the number of time harmonics is increased, the amplitude of lower harmonics becomes closer and closer to that of the corresponding harmonic in the reference signal, and errors move toward the higher resolved harmonics. For $N = 20$, the amplitudes of the 20 resolved harmonics are similar for both the time and space spectra.

In summary, the preceding analysis shows that, for under-resolved HB computations, the time signal is affected by both amplitude and phase errors, since the energy content is redistributed incorrectly among the resolved harmonics.

To quantify this error, we apply the error measure defined in Eq. (36) , to HB computations of the model turbomachinery problem corresponding to different choices of the wake thickness and different numbers of harmonics. Results are presented in Fig. 19. The ε_2 error map is qualitatively and quantitatively similar to the ε_1 discussed in the previous section. Again, the truncation error measured

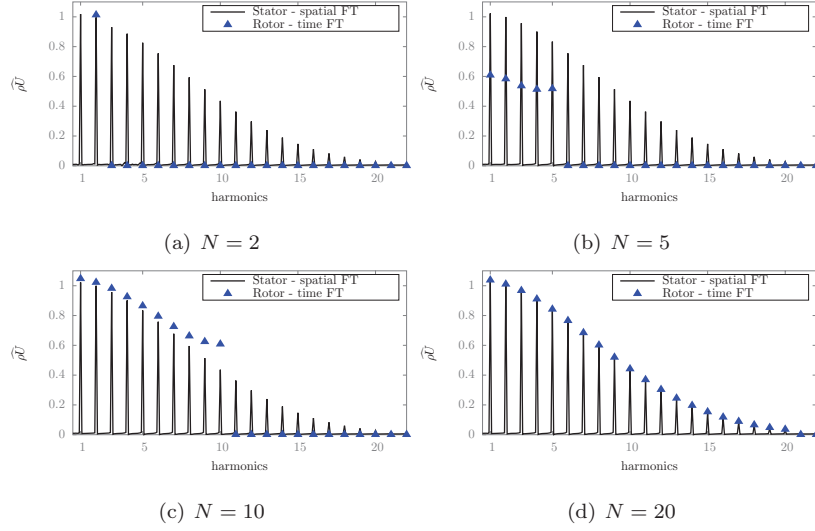(a) $N = 2$

(b) $N = 5$

(c) $N = 10$

(d) $N = 20$

Figure 18: Spatial/time duality for a $L = 5\%$ wake width.

using ε_2 for thick wakes and high numbers of harmonics does not follow the trend observed for the theoretical error ε_{th}, due to the spatial filtering introduced at the interface by the phase-lag condition.

The preceding analysis shows that, for HB computations that are well converged in terms in harmonics, the spatial spectrum in the stator and the time spectrum in the rotor block tend to match, except for additional spatial errors introduced by the use of an azimuthal Fourier transform on a bounded interval, which confirms the validity of the error measure defined in Eq. (36).

4.4. Comparison with the theoretical error measure

The preceding results show that approximated truncation error measures computed for the model turbomachinery problem using a nonlinear flow model (Euler equations) exhibit trends, with respect to the wake thickness and number of HB harmonics, in close agreement with the theoretical error measure derived in Section 3.3 for a Gaussian function. Figure 20 compares the different error measures for HB simulations of advected wakes of varying thickness versus the number of harmonics used for the time discretization. This corresponds to
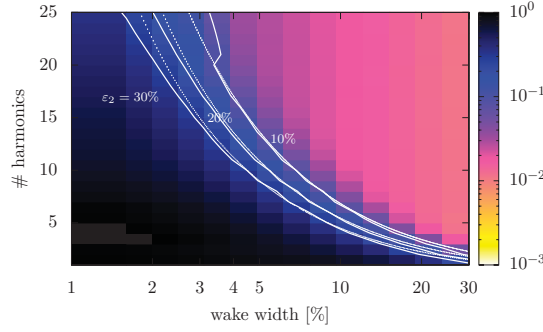
Figure 19: Evaluation of the error due to the wake capturing using the second error quantification (ε_2), and comparison with analytical error (dotted lines).

horizontal cuts of Figs 9, 14 and 19. For a number of harmonics higher than the cutoff harmonic used in the phase-lag condition the three error measures give results in very close agreement. After that value, both the ε_1 and ε_2 error measures applied to the model turbomachinery problem exhibit a plateau. The same plateau is also observed on ε_{mxp} error whose definition will be given in the next section. The preceding remarks suggest the idea that, since all error measure provide similar results, at least up to numbers of harmonics of interest for practical applications. An *a priori*, an a priori estimate of the number of harmonics required to achieve a given error level could then be obtained by using the theoretical error measure Eq. (29), if a quick estimate of the wake thickness characteristic of a given turbomachinery problem is available. In the next section, we show that a reasonable estimate of the convergence of the error can be obtained from a preliminary steady computation based on the mixing plane interface condition.

4.5. Toward an a priori~~priori~~ error estimate

In order to define an *a priori* error measure that can be used to estimate the number of harmonics required to achieve a reasonable convergence of the HB method, we suggest to evaluate the wake thickness by using a preliminary mixing plane steady computation. Indeed, if potential effects due to the downstream row can be neglected, the spatial information at the interface in the
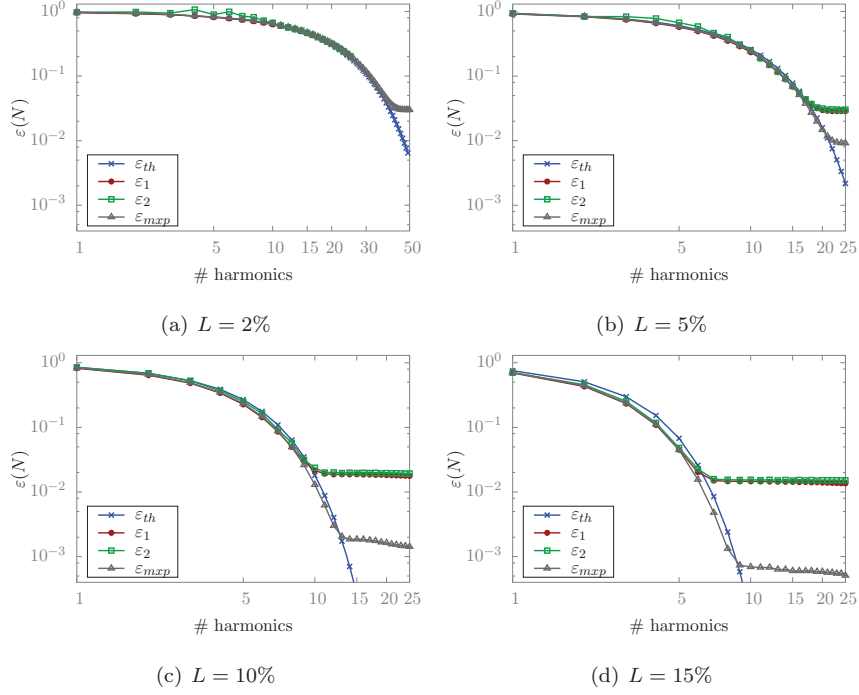
31

Figure 20: Truncation, computed and analytical errors for four wake widths~~width~~.

stator block, essentially due to the incoming wakes, can be captured without taking into account the relative motion between the wheels, *i.e.* by means of a mixing plane computation. Given the approximated azimuthal distribution at the stator interface, we consider the cumulative energy content of the signal up to a given frequency f (or, equivalently, to a given harmonic $N = f/f_1$ where f_1 is the frequency value of the considered unsteadiness). The cumulative energy is defined as:

$$E(f) = \frac{\int_0^f |\widehat{g}(\zeta)|^2 \, \mathrm{d}\zeta}{\int_0^\infty |\widehat{g}(\zeta)|^2 \, \mathrm{d}\zeta}, \tag{37}$$

where $\widehat{g}$ is the spectrum of the quantity of interest , here the axial momentum. By comparison with Eq. (23), the relation between the relative accumulated energy E and the truncation error ε_{mxp} is:

$$E(f) = 1 - \varepsilon_{mxp}^2(f). \tag{38}$$

Note that this last error measure is based only on the amount of unresolved

energy that is left in a computation if the spatial signal is truncated at a given cutoff frequency f, and does not require any information from the rotor block. In fact, ~~, but~~ it depends only on the characteristics of the incoming wake.

To check if the new error measure represents an accurate estimate of the truncation error of an HB simulation, we carry out again a parametric study of the error versus different wake thicknesses and numbers of harmonics (equivalently, cutoff frequencies), and compare the results to those of the *a posteriori* error measures obtained for the model turbomachinery problem (ε_1, ε_2) and to~~for~~ the theoretical error ε_{th}. Results corresponding to ε_{mxp} are superposed to the corresponding curves in Fig. 20. The *a priori* error measure (ε_{mxp}) matches the theoretical estimate (ε_{th}) and the *a posteriori* measures (ε_1, ε_2) over a wide range of harmonics. Similarly to the *a posteriori* errors ε_1 and ε_2, the *a priori* error ε_{mxp} exhibits a plateau for high N and high wake thicknesses, due to the application of the Fourier transform on a bounded interval. We also stress the close agreement between ε_{mxp} and ε_{th}: specifically, estimates of the number of harmonics needed to capture 99% of the cumulative energy (equivalently, to get a truncation error equal to 10% whom value will be justified later) are identical for all error measures.

5. Application to a contra-rotating open rotor configuration

Originally, this study was conducted to understand the convergence issues observed on Contra-Rotating Open Rotor (CROR) configurations. In contrast to turbomachinery applications, convergence in terms of harmonics has been observed to be slow on some configurations.

5.1. Presentation of the cases

To investigate this issue, two CROR configurations are studied at different operating conditions:

1. a Mock-up CROR (noted MU) designed by Safran to be investigated in a wind tunnel (*i.e.* ground condition: $P_i = 101,300$ Pa and $T_i = 293$ K).

Two regimes are considered representative of low (LS) and high-speed (HS) conditions (different rotation speeds and blade angles),

2. the Airbus-designed AI-PX7 CROR (noted AI) at cruise condition: high-speed and flight level (*i.e.* $P_i = 23,842$ Pa and $T_i = 219.6$ K).

5.2. Results of HB computations

Figures 21, 22 and 23 show the non-dimensional entropy at 75% span computed by the HB method for the three configurations. The MU-LS configuration has the fastest convergence. There are indeed some spurious entropy waves downstream the blade row interface for $N = 1$ and 2 but none are observed starting $N = 4$.

| (a) $N = 1$ | (b) $N = 2$ | (c) $N = 3$ |

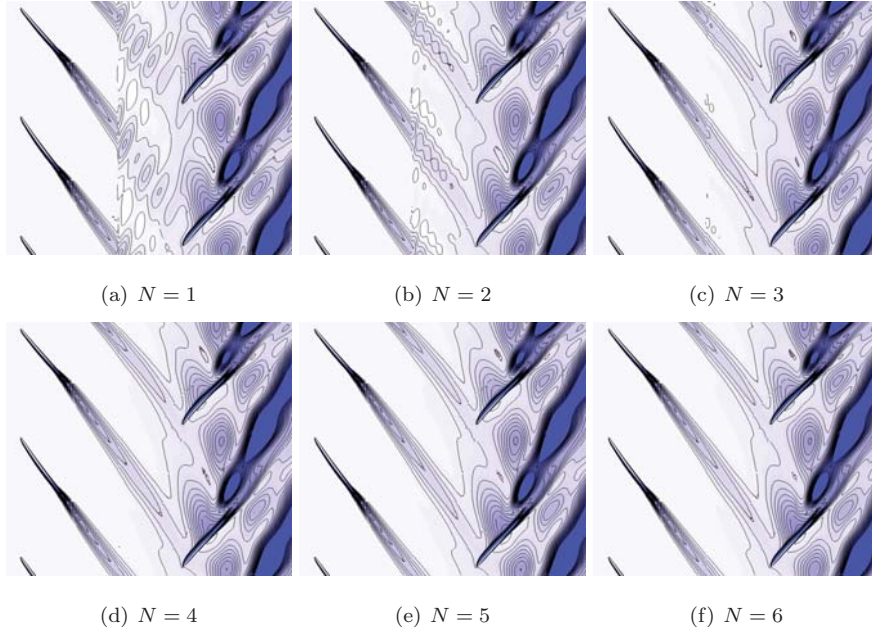| (d) $N = 4$ | (e) $N = 5$ | (f) $N = 6$ |

Figure 21: MU-LS convergence – Non-dimensional entropy at 75% span.

For the MU-HS configuration, one can observe in Fig. 22(g) that the $N = 7$ HB computation still presents some spurious waves downstream the interface. It becomes negligible for a finer sampling. The main difference with the MU-LS configuration is the blade angle. By comparing Fig. 21 and Fig. 22, one

can observe that the blade angle is lower in the high-speed case. Therefore, even if the wake is of similar thickness downstream the front rotor, it impacts the axial blade row interface with a lower angle and therefore looks thinner. Assuming that the flow angle downstream the trailing edge is the same as the blade incidence angle ξ, the wake thickness observed by the blade row interface L_{itf} is

$$L_{itf} = \frac{L}{\cos(\xi)}. \tag{39}$$

When ξ rises from low-speed to high-speed configuration, L will remain almost constant but L_{itf} will decrease and the spectrum widens.

For the AI configuration, Fig. 23 shows that the convergence is not achieved as the finest HB computation ($N = 10$) still not capture correctly the wake through the interface. It is thickened by the low time resolution. Although the solver is able to account for an arbitrary number of time samples, the required memory would lead to run on more processors and thus block splitting would become necessary. As the advantage over classical time-marching scheme would vanish, only $N = 1$ to 10 HB simulations were performed.becomes too demanding and only $N = 1$ to 10 were attempted.

The observed convergence differences between the AI and MU-HS configurations can be attributed to two main differences: The are two main differences with the MU-HS configuration:

1. the AI configuration is at scale meaning that the radial extent is several times larger than the MU configuration. As the pitchwise relative wake width is defined as

$$L_{pitch} = L\frac{B}{2\pi R}, \tag{40}$$

the relative wake width will decrease for higher radius R. It also explains the difference with classical turbomachinery: as the number of blades B can be one order of magnitude higher in the latter case than in a CROR configuration and the diameter lower, the relative wake thicknesses are higher and the spectrum narrower.

(a) $N = 1$ (b) $N = 2$ (c) $N = 3$

(d) $N = 4$ (e) $N = 5$ (f) $N = 6$

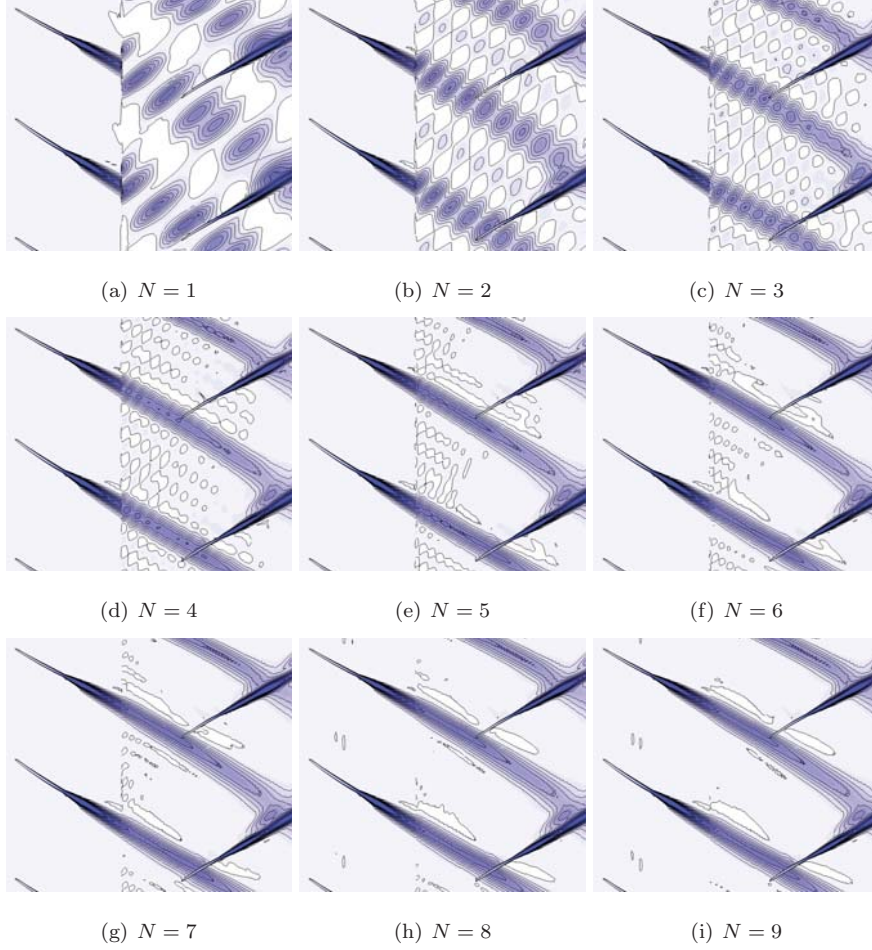(g) $N = 7$ (h) $N = 8$ (i) $N = 9$

Figure 22: MU-HS convergence – Non-dimensional entropy at 75% span.

2. the viscosity is also different: applying the Sutherland law for air at ground and flight level leads to dynamic viscosities of ~~respectively,~~ $1.807 \cdot 10^{-5}$ Pa.s and $1.434 \cdot 10^{-5}$ Pa.s, respectively. With lower viscosity, the blade boundary layer is thinner and the generated wakes are thinner as well. Furthermore, the mixing with the main flow is weaker and the thickening of the wakes is also slower leading to a thinner wake reaching the blade row interface.
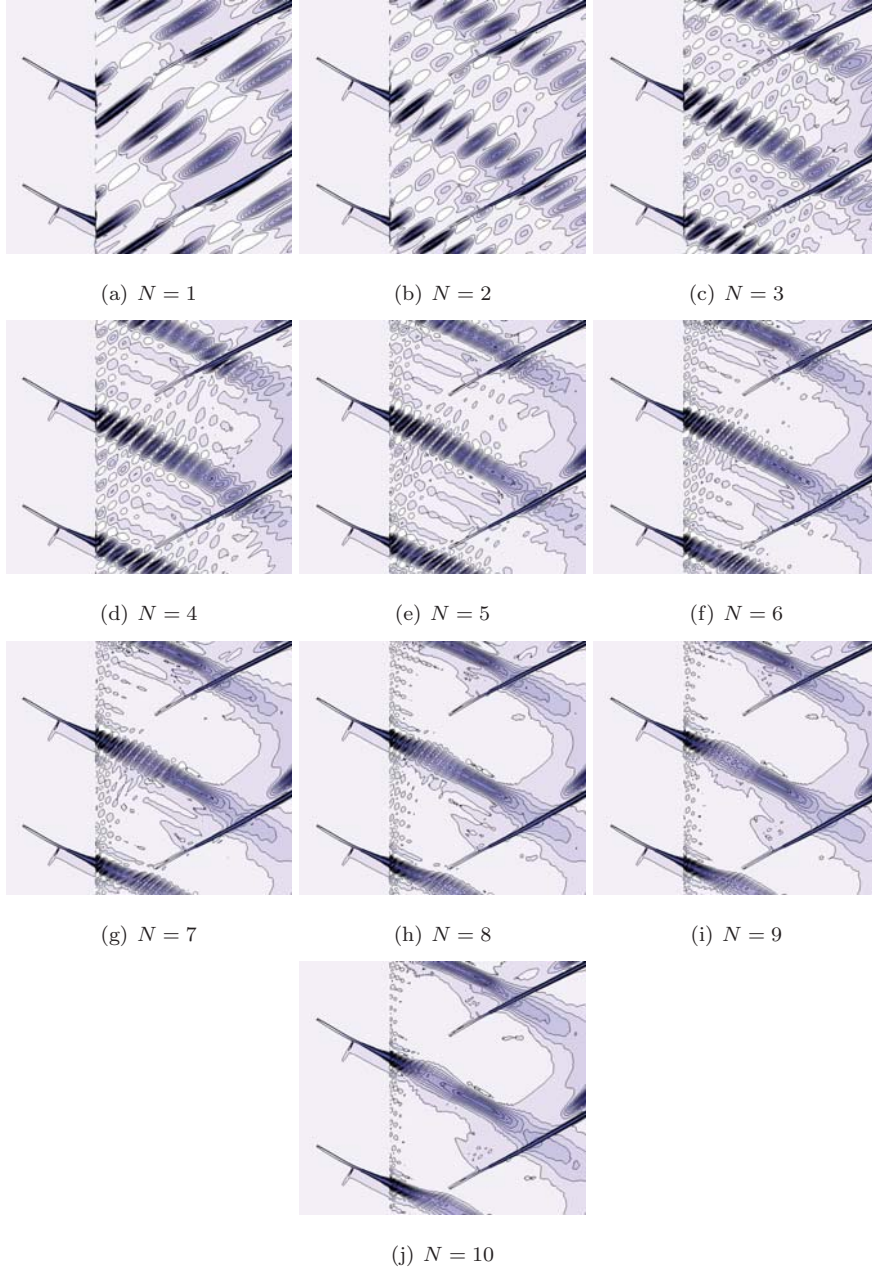
(a) $N = 1$

(b) $N = 2$

(c) $N = 3$

(d) $N = 4$

(e) $N = 5$

(f) $N = 6$

(g) $N = 7$

(h) $N = 8$

(i) $N = 9$

(j) $N = 10$

Figure 23: AI-HS convergence – Non-dimensional entropy at 75% span.

5.3. Prediction tool based on the wake thickness

To estimate the wake thickness, a curve fitting algorithm is used to fit the CFD wakes to the Lakshminarayana and Davino Gaussian wake law. Only the relative span between 10% and 70% is considered as elsewhere, the wake interacts with the hub boundary layer and tip vortex. This estimation is plotted in Fig. 24 for the three configurations. The wake thickness is almost constant
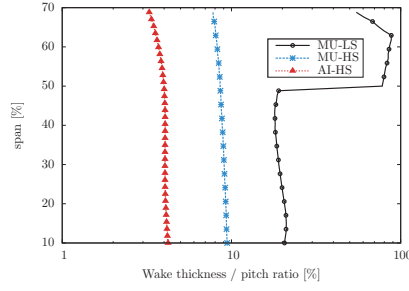

Figure 24: Estimation of the relative wake thickness for the three contra-rotating open rotor configurations.

along the span for the two HS configurations. In opposite, the MU-LS shows an increase at 50% of the relative span. This is due to a large tangential distortion that is attributed to flow separation. Thus, the wake width estimation is not reliable in this region for the MU-LS configuration as the tangential distortion is no longer Gaussian-shaped. Nevertheless, using Fig. 24, the wake widths of the AI-HS, the MU-HS and the MU-LS are approximately 4%, 9.5% and 20%, respectively.

At this point, using the theoretical error defined in Eq. (29), the last thing needed to provide an estimation of the required number of harmonics, is the level of accumulated energy (or alternatively the level of error) that ensures the convergence of the HB method. The level of accumulated energy (defined in Eq. (37)) required for a computation to be rigorously converged is difficult to estimate. It seems reasonable, from an engineering standpoint, to consider that a 99% accumulation of energy should be a good criterion. To emphasize that, the reconstruction of a wake as a function of four levels of cumulative energy

E is depicted in Fig. 25. One can see that a reconstruction using only 50%
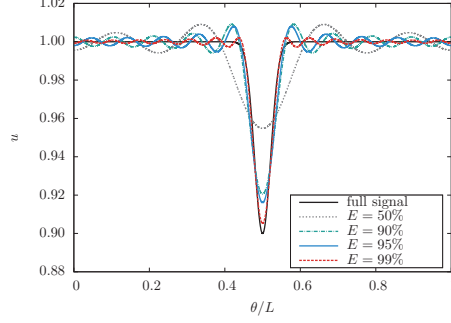

Figure 25: Reconstructions of a wake depending on the energy content kept in the signal.

of the energy leads to a signal that has neither the right wake deficit nor the correct width. Using 90% and 95% of the energy improve the resulting shape but large secondary oscillations remain, with a bad capture of the wake deficit. In opposite, by using 99% of the energy to reconstruct the signal, only minor oscillations are seen but the wake width and deficit are recovered with more than 95% accuracy. Thus, the 99% energy threshold ensures that the wake will be correctly transmitted to the opposite row, which is the prior concern of this paper. Therefore, based on this value and the estimation of the wake width for all the three CROR configurations shown in Fig. 24, one can evaluate the number of harmonics needed to compute such applications. In fact, based on the analytic formula derived in Sec. 3.3 and the equivalence of truncation error and accumulated energy given by Eq. (38), one can deduce the number of harmonics N needed to capture a target level of accumulated energy E for a given wake width:

$$N(E) = \frac{\mathrm{erfc}^{-1}\left[1 - E\right]}{\sqrt{2\alpha'}}, \tag{41}$$

where α' is the wake parameter as defined in Sec. 3.3:

$$\alpha'(L) = \frac{1}{0.693}\left(\frac{\pi L}{2}\right)^2. \tag{42}$$

Here, the theoretical estimation of the number of harmonics needed to recover 99% of the energy is then 17, 7 and 3 for, respectively, the AI-HS, the MU-

HS and the MU-LS. These numbers explain why the AI-HS configuration is still not converged after $N = 10$ harmonics. In fact, such a computation leads to a capture of~~recover~~ only 87% of the signal energy. Figure 25 supports the argument that with this level of energy, the wake is not properly captured as a 90% energy signal does not accurately estimate the wake deficit and thickness.

With this approach, one can deduce approximately the number of harmonics needed to compute such CROR configurations using Fourier-based time methods for a target level of accumulated energy. However it is limited to Gaussian wakes. If the wake shape is very far~~different~~ from a Gaussian curve or if another tangential distortion reaches the interface, the present prediction tool cannot be used. However, as demonstrated in Sec. 4.4, the analytic error and the error based on an azimuthal Fourier transform of the distortion seen just upstream the interface for a mixing-plane configuration are equivalent.

5.4. Prediction tool based on an azimuthal Fourier transform

Thus, a more general way to analyze the spectrum in a wake is to perform an azimuthal Fourier transform at the rows interface in a mixing-plane computation. It encompasses both the wake analysis done above and also any tangential disturbances, as for instance the viscosity effects near the hub or the tip vortex. Details of the algorithm used to compute the tangential accumulated energy from a mixing plane computation are given in Appendix C.

To have a global insight of the energy contained in the tangential distortion across the whole span, the energy accumulation is plotted using a color map in Fig. 26. Three contour lines are added to ease the interpretation: 90%, 95% and 99% of accumulated energy, corresponding to a truncation error of respectively 30%, 20% and 10%. The richer spectrum is observed in the wake region between 10% and 70% of relative span. This is the region where the wake is influenced neither by the hub boundary layer nor by the tip vortex. Therefore the wake drives the convergence of HB computations. Results are in good agreement with the prediction tool based on the wake thickness. To emphasize that, the number of harmonics needed to have 99% of the energy is given in Tab. 1 for a relative
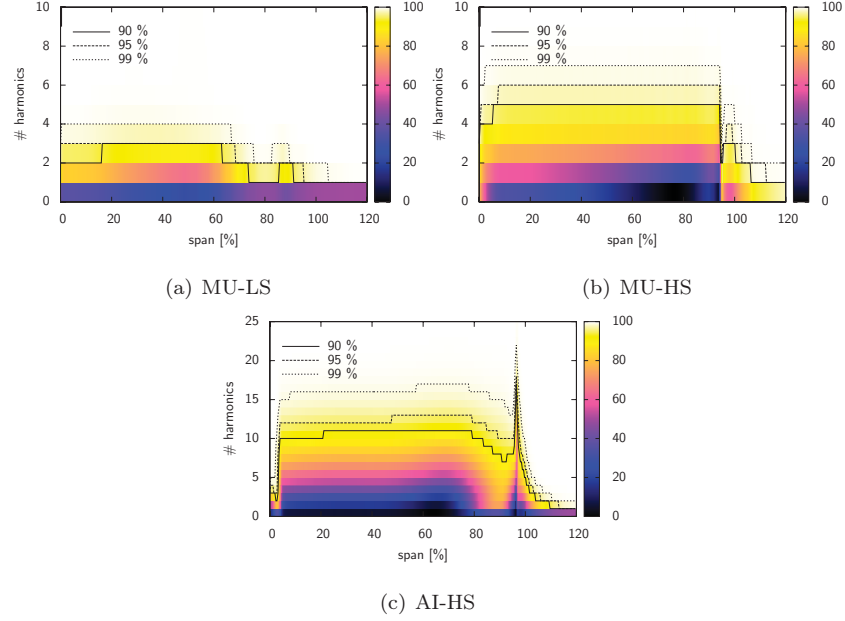
(a) MU-LS

(b) MU-HS

(c) AI-HS

Figure 26: Energy accumulation by harmonics for all spans.

span between 10% and 70%.

configuration	AI-HS	MU-HS	MU-LS
wake thickness	17	7	3
azimuthal Fourier transform	16	7	4

Table 1: Predicted number of harmonics associated to $E = 99\%$ of accumulated energy, using two prediction tools, the first based on the wake thickness and the second based on an azimuthal Fourier transform.

Figure 27 shows the non-dimensional axial momentum extracted at the rotor/rotor interface from a single-passage mixing-plane computation for the three considered configurations. One can observe different wake shapes: the AI High-Speed (HS) wake looks much thinner than the MU-HS, which looks thinner than the Low-Speed (LS) one. Indeed, the latter does not show a well delimited wake structure all along the span explaining the estimation of the number of harmonics needed to capture such configurations.

41

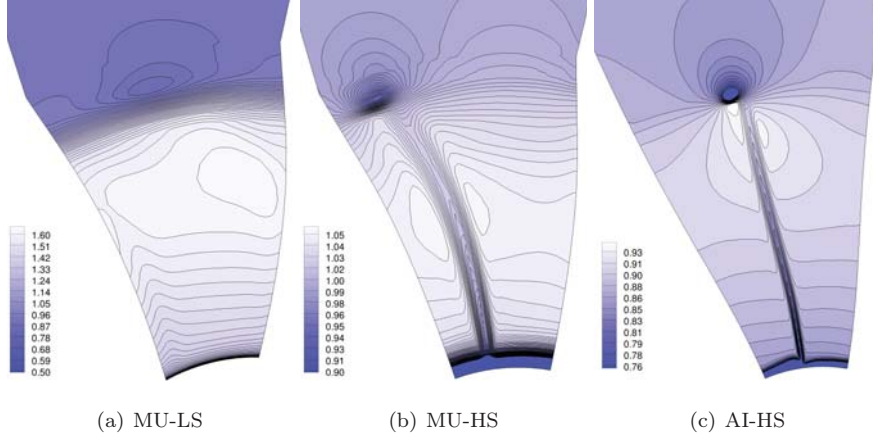|		
(a) MU-LS	(b) MU-HS	(c) AI-HS

Figure 27: Non-dimensional axial momentum $(\rho U)/(\rho U)_\infty$ at the rotor/rotor interface (mixing-plane computations).

This prediction tool is more accurate as it handles wake tangential distortion as well as any other type of azimuthal distortions. Thus, it can be used to predict the number of harmonics needed to capture a certain level of energy for any relative span. The computational time needed to get the accumulated energy pictures as in Fig. 26 is negligible. In fact, it takes less than a minute.

We verify *a posteriori* that the number of harmonics provided in Tab. 1 are sufficient to yield converged HB computations. For the MU-LS, the prediction tool estimate that four harmonics are sufficient. In fact, Fig. 21 supports the argument that four harmonics gives a converged simulation as the difference between $N = 4$, $N = 5$ and $N = 6$ HB computations are barely visible. For the MU-HS, seven harmonics are estimated to be sufficient while visually, it seems that $N = 8$ is converged. In fact, one must keep in mind that these criteria just give a lower bound of the required number of harmonics needed to get the convergence of the HB method. Indeed, when running a N-harmonic HB computation, the time period is sampled with $2N + 1$ time instants which is, according to the Nyquist-Shannon criteria [25, 26], the minimum sampling to get the Nth of the fundamental frequency. It does not necessarily mean that the level of the Nth harmonic is accurately predicted. Experience shows that

in order to reach this level, one has sometimes to run a $N + 1$ or $N + 2$ HB computation.

6. Conclusions

The accuracy and efficiency of Fourier-based time methods used to solve periodic unsteady problems depends on the number of harmonics chosen to represent the frequency content of the time signal. In this work we investigate the accuracy and convergence properties of Fourier-based time integration methods. The convergence rate of these methods, in terms of harmonics required to describe the solution with a given level of accuracy, depends on the spectral content of the solution itself: Fourier-based time methods are particularly efficient for flow problems characterized by a narrow Fourier spectrum. Starting from this remark, we try to define a relevant indicator of solution regularity in the specific case of turbomachinery flows, which represent one of the main applications of Fourier-based time methods in Fluid Mechanics. To this aim, we show that the main source of unsteadiness in turbomachinery flows is due to the relative motion of wakes generated by a given blade row with respect to the downstream row. Statistically speaking, the passing wakes can be~~are~~ seen by the downstream row as an azimuthally advected periodic Gaussian pulse, characterized by its relative thickness compared to the pitch in between two subsequent blades and by the velocity deficit associated to it. We show that the narrower the wake, the larger its Fourier spectrum, and the slower the convergence of Fourier-based time methods. In order to achieve *a priori*~~a priori~~ estimates of the number of harmonics required to accurately solve a given turbomachinery problem~~, we introduce two error measures based on the relative thickness of the passing wakes. It is shown that, for practical purposes, these can be preliminary estimated by running a companion steady simulation of the turbomachinery stage. The~~ a steady (mixing-plane) simulation is post-processed to extract ~~information about the spanwise distribution of wake thickness~~ tangeantial variations and the corresponding spectrum upstream the blade row interface and an error criterion is

used to estimate the number of harmonics required to resolve 99% of the energy content associated to the velocity signal. The preliminary step has a negligible cost compared to the overall simulation, since the steady computation is used to initialize the unsteady run, and extraction of wake characteristics takes less than a minute on a single processor.

The proposed methodology represents an efficient and reliable operational tool to guide the choice of the number of harmonics for a given turbomachinery problem, and to evaluate beforehand the interest of applying or not a Fourier-based time integration scheme instead of a classical time-marching scheme.

Acknowledgments

Appendix A. Detailed algorithm to compute ε_1

A sketch of the steps used to evaluate ε_1 from a computation is shown in Fig. A.28. Two azimuthal lines are extracted in the stator and in the rotor respectively (step ①). These are duplicated using the phase-lag condition to retrieve the full 2π signal in both blocks. The axial momentum ρU variable is analyzed. The main advantages of this variable are that it is a representative variable for the wake, it is a conservative variable of the considered governing equations and finally, it is invariant under a change of reference frame, unlike the relative velocities for instance. Then, an azimuthal Fourier transform, denoted $\mathcal{F}_\theta$, is carried out on each azimuthal 2π signals and gives the frequency content of the wake in both the stator and the rotor (step ②). However, due to the time interpolation between the two rows achieved at the interface, spurious effects can
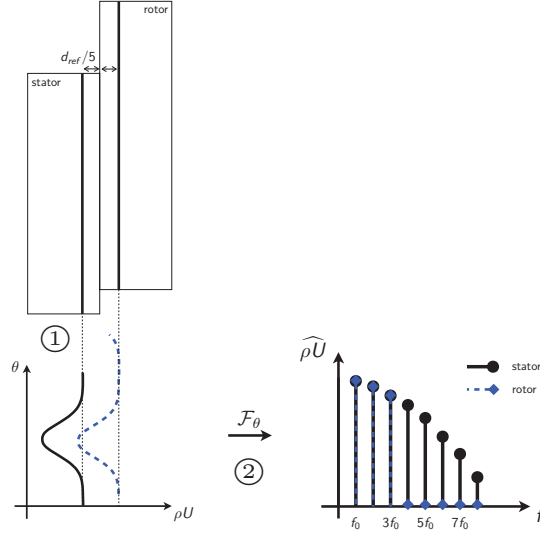
Figure A.28: Sketch of the steps needed to compute the first error quantification ε_1.

appear upstream the interface as shown in Fig. A.29. For instance, t~~T~~he effects of the rotor block are significant on the closest cells to the interface for the $N = 5$ computation and still appear on the very lasts cells before the interface for the $N = 10$ computation. They have disappeared when using $N = 15$ harmonics. To lessen the influence of this interpolation, and thus the spurious effects, the extraction of the axial momentum is not performed at the closest cell to the interface. If d_{ref} is the axial length of a block, the extraction is achieved at $d_{ref}/5$ of the interface upstream and downstream the stator and rotor block, respectively. It represents six time the length of a cell in the axial direction. As the governing equations are the Euler ones, there is no significant variation of the wake thickness within six cells, which supports this hypothesis~~supporting this approach~~. Moreover, preliminary studies have shown that $d_{ref}/5$ is sufficient to lower the spurious effects while keeping the results consistent.
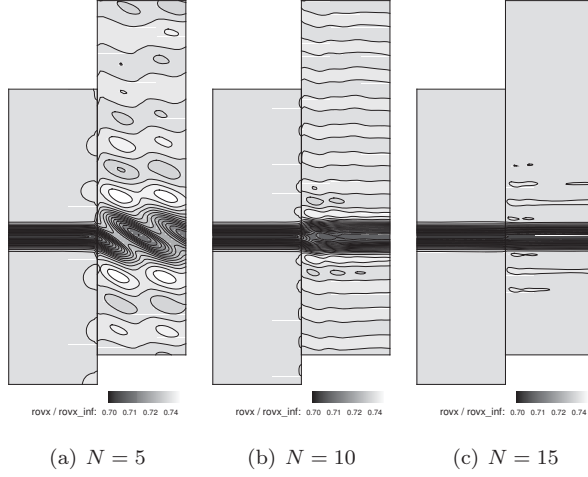
(a) $N = 5$ (b) $N = 10$ (c) $N = 15$

Figure A.29: Occurrence of spurious effects upstream the interface between stator and rotor blocks for a $L = 5\%$ wake width.

Appendix B. Detailed algorithm to compute ε_2

The steps to compute the second error quantification for each of the 375 computations, are schematically shown in Fig. B.30. An azimuthal line is extracted in the stator domain, nearby the interface (step ①), as for the first error quantification. However, in the rotor block, a time probing is done at one point giving an unsteady time signal of $\rho U(t)$ (step ①′). The azimuthal signal is duplicated using the phase-lag condition to retrieve the full 2π signal. The temporal and spatial signals are then Fourier transformed so that their spectrum can be compared (step ②). The wake extraction is performed at the same axial distance of the interface as for the first error quantification. In this case, the location of the point in the rotor block has a direct impact on the results especially when the wake is under-resolved. To highlight this impact, the temporal Fourier transform is evaluated at two different locations called loc 1 and loc 2. The two points are separated by a distance $\Delta\theta_{loc_1-loc_2} = d_{ref}/10$ in the azimuthal direction, as shown in Fig. B.30.
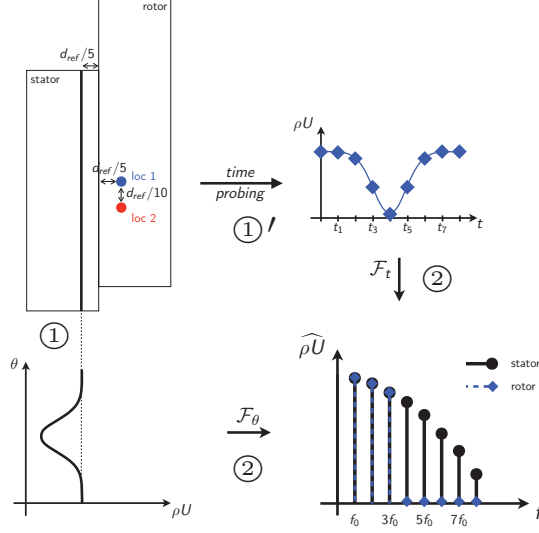
Figure B.30: Sketch of the steps needed to compute the second error quantification.

Appendix C. Detailed algorithm to the tangential accumulated energy from a mixing plane computation

Figure C.31 shows the different steps: firstly, the row interface is extracted from a mixing-plane computation. Secondly, using this interface, the axial momentum is extracted for several spanwise positions in the region of interest (step ①). In a CROR configuration this is the region with a relative span ranging between 0% and 120%. In fact, beyond the 120% threshold, the influence of the blades on fluid unsteadiness decreases rapidly such that the fluid has a narrow spectrum as the whole spectrum energy lies in the first, at most, the first three harmonics. Then, for each radii, an azimuthal Fourier transform is performed to obtain the tangential spectrum of the axial momentum (step ②). The relative cumulative energy for a given number of harmonic N is then defined as:

$$E(N) = \frac{\sum_{k=1}^{N} \left[\widehat{\rho U}^{\theta}(k) \right]^2}{\sum_{k=1}^{\infty} \left[\widehat{\rho U}^{\theta}(k) \right]^2}, \tag{C.1}$$
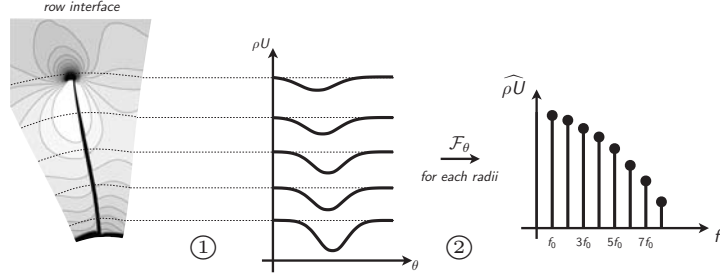
Figure C.31: Steps for the prediction tool based on an azimuthal Fourier transform of the axial momentum at the rotor-rotor interface.

where $\widehat{\rho U}^{\theta}$ denotes the axial momentum spectrum extracted from the rows interface plane. In Eq. (C.1), the cumulative energy up to harmonic N is compared to the total energy.

References

[1] L. He, Fourier Methods for Turbomachinery Applications, Progress in Aerospace Sciences 46 (8) (2010) 329–341. doi:10.1016/j.paerosci.2010.04.001.

[2] L. He, W. Ning, Efficient Approach for Analysis of Unsteady Viscous Flows in Turbomachines, AIAA Journal 36 (11) (1998) 2005–2012. doi:10.2514/2.328.

[3] W. Ning, L. He, Computation of Unsteady Flows Around Oscillating Blades Using Linear and Nonlinear Harmonic Euler Methods, Journal of Turbomachinery 120 (3) (1998) 508–514. doi:10.1115/1.2841747.

[4] K. C. Hall, J. P. Thomas, W. S. Clark, Computation of Unsteady Nonlinear Flows in Cascades using a Harmonic Balance Technique, AIAA Journal 40 (5) (2002) 879–886. doi:10.2514/2.1754.

[5] A. Gopinath, A. Jameson, Time Spectral Method for Periodic Unsteady Computations over Two- and Three- Dimensional Bodies, in: 43rd

Aerospace Sciences Meeting and Exhibit, AIAA Paper 2005-1220, Reno, NV, USA, 2005. doi:10.2514/6.2005-1220.

[6] T. Guédeney, A. Gomar, F. Gallard, F. Sicot, G. Dufour, G. Puigt, Non-Uniform Time Sampling for Multiple-Frequency Harmonic Balance Computations, Journal of Computational Physics 236 (2013) 317–345. doi:10.1016/j.jcp.2012.11.010.

[7] F. Sicot, G. Dufour, N. Gourdain, A Time-Domain Harmonic Balance Method for Rotor/Stator Interactions, Journal of Turbomachinery 134 (1) (2012) 011001. doi:10.1115/1.4003210.

[8] G. Dufour, F. Sicot, G. Puigt, C. Liauzun, A. Dugeai, Contrasting the Harmonic Balance and Linearized Methods for Oscillating-Flap Simulations, AIAA Journal 48 (4) (2010) 788–797. doi:10.2514/1.43401.

[9] C. Canuto, M. Y. Hussaini, A. Quarteroni, T. A. Zang, Spectral methods: Fundamentals in single domains, Springer, 2006.

[10] A. Zygmund, Trigonometric series, Vol. 1, Cambridge university press, 1959.

[11] S. Vilmin, C. Hirsch, E. Lorrain, M. Swoboda, Unsteady Flow Modeling across the Rotor/Stator Interface Using the Nonlinear Harmonic Method, in: ASME Turbo Expo: Power for Land, Sea and Air, Vol. 6: Turbomachinery, Parts A and B, Barcelona, Spain, 2006, pp. 1227–1237. doi:10.1115/GT2006-90210.

[12] K. Ekici, K. C. Hall, R. E. Kielb, Harmonic Balance Analysis of Blade Row Interactions in a Transonic Compressor, Journal of Propulsion and Power 26 (2) (2010) 335–343. doi:10.2514/1.43879.

[13] M. McMullen, A. Jameson, J. Alonso, Acceleration of Convergence to a Periodic Steady State in Turbomachinery Flows, in: 39th Aerospace Sciences Meeting and Exhibit, AIAA Paper 2001-0152, Reno, NV, USA, 2001. doi:10.2514/6.2001-152.

[14] M. McMullen, A. Jameson, J. Alonso, Application of a Non-Linear Frequency Domain Solver to the Euler and Navier-Stokes Equations, in: 40th AIAA Aerospace Sciences Meeting and Exhibit, AIAA Paper 2002-0120, Reno, NV, USA, 2002. doi:10.2514/6.2002-120.

[15] M. McMullen, A. Jameson, The Computational Efficiency of Non-Linear Frequency Domain Methods, Journal of Computational Physics 212 (2) (2006) 637–661. doi:10.1016/j.jcp.2005.07.021.

[16] F. Sicot, G. Puigt, M. Montagnac, Block-Jacobi Implicit Algorithms for the Time Spectral Method, AIAA Journal 46 (12) (2008) 3080–3089. doi:10.2514/1.36792.

[17] E. van der Weide, A. Gopinath, A. Jameson, Turbomachinery Applications with the Time Spectral Method, in: 35th AIAA Fluid Dynamics Conference and Exhibit, AIAA Paper 2005-4905, Toronto, ON, Canada, 2005. doi:10.2514/6.2005-4905.

[18] A. Jameson, W. Schmidt, E. Turkel, Numerical Solutions of the Euler Equations by Finite Volume Methods Using Runge-Kutta Time-Stepping Schemes, in: AIAA 14th Fluid and Plasma Dynamic Conference, AIAA-81-1259, Palo Alto, CA, USA, 1981.

[19] B. Lakshminarayana, R. Davino, Mean Velocity and Decay Characteristics of the Guidevane and Stator Blade Wake of an Axial Flow Compressor, Journal of Engineering for Power 102 (1) (1980) 50–60. doi:10.1115/1.3230231.

[20] J. I. Erdos, E. Alznert, W. McNally, Numerical Solution of Periodic Transonic Flow through a Fan Stage, AIAA Journal 15 (11) (1977) 1559–1568. doi:10.2514/6.1976-369.

[21] G. A. Gerolymos, V. Chapin, Generalized Expression of Chorochronic Periodicity in Turbomachinery Blade-Row Interaction, La Recherche Aérospatiale 5 (1991) 69–73.

[22] L. Cambier, S. Heib, S. Plot, The Onera Elsa CFD Software: Input from Research and Feedback from Industry, Mechanics & Industry 14 (03) (2013) 159–174. doi:10.1051/meca/2013056.

[23] D. Hassan, F. Sicot, A Time-Domain Harmonic Balance for Dynamic Derivatives Predicitons, in: 49th AIAA Aerospace Sciences Meeting, Orlando, FL, USA, 2011. doi:10.2514/6.2011-1242.

[24] P. L. Roe, Approximate Riemann Solvers, Parameter Vectors and Difference Schemes, Journal of Computational Physics 43 (2) (1981) 357–372. doi:10.1016/0021-9991(81)90128-5.

[25] H. Nyquist, Certain Topics in Telegraph Transmission Theory, Transactions of American Institute of Electrical Engineers 47 (1928) 617–644. doi:10.1109/T-AIEE.1928.5055024.

[26] C. E. Shannon, Communication in the Presence of Noise, Proceeding of the Insitute of Radio Engineers 37 (1) (1949) 10–21. doi:10.1109/JPROC.1998.659497.